COMOTI
ROMANIAN RESEARCH & DEVELOPMENT INSTITUTE FOR GAS TURBINES

TURBO

Scientific Journal

vol. VIII (2021), no. 2

On 31 March 2021, the European Space Agency is opening the application process for **its first astronaut** selection in over a decade.

COMOTI is proud of Theodora ANDREESCU.

She was accepted for ESA first astronaut selection!

Editorial Board

PRESIDENT:
Dr. Eng. Valentin SILIVESTRU

VICE-PRESIDENT:
Dr. Eng. Romulus PETCU
Dr. Eng. Cristian CARLANESCU

TECHNICAL SECRETARY:
Dr. Eng. Jeni VILAG

MEMBERS:
Prof. Dr. Virgil STANCIU
Prof. Dr. Corneliu BERBENTE
Prof. Dr. Dan ROBESCU
Prof. Dr. Sterian DANAILA
Conf. Dr. Eng. Daniel-Eugeniu CRUNTEANU
Conf. Dr. Eng. Grigore CICAN
Mat. Dr. Eng. Catalin NAE
Dr. Eng. Gheorghe MATACHE
Dr. Eng. Ene BARBU
Dr. Eng. Gheorghe FETEA
Dr. Eng. Valeriu VILAG
Dr. Eng. Ionuț PORUMBEL
Dr. Eng. Valeriu DRAGAN
Dr. Eng. Lucia Raluca MAIER
Dr. Eng. Andreea MANGRA
Dr. Eng. Sorin GABROVEANU

EDITOR IN CHIEF:
Prof. Dr. Lacramioara ROBESCU

EDITORS:
Dr. Eng. Mihaela Raluca CONDRUZ
Ec. Elena BANEA

ADMINISTRATIVE SECRETARY:
Eng. Mihaela GRIGORESCU

TRANSLATION CHECKING:
Dr. Eng. Ionut PORUMBEL
Oana HRITCU

GRAPHICS:
Victor BESLEAGA

More information:
http://www.comoti.ro/ro/jurnalul_stiintific_turbo.htm
jeni.vilag@comoti.ro

ISSN: 2559-608X
ISSN-L: 1454-2897

Scientific Journal TURBO is included in:
-ICI World of Journals:
ICV 2020: 60,04
https://journals.indexcopernicus.com/search/details?id=48512

-Directory of Open Access Scholarly Resources (ROAD)
https://portal.issn.org/resource/ISSN/2559-608X#

-Directory of Research Journals Indexing (DRJI):
http://olddrji.lbp.world/JournalProfile.aspx?jid=2559-608X

CONTENT

- Editorial 2

AUTOMATION AND MONITORING:

- Passengers Monitoring System with Infrared Sensors and Microcontroller
D. Lale, C. Borzea, S. Gogoneata, C. Nechifor, M. Vasile, F. Niculescu 4

COMPRESSORS, BLOWERS, TURBINES :

- Coupling Torsional Vibration Analysis of a Screw Compressor - Caterpillar Engine System
I. Vladuca, R. Ionescu, C. G. Petre, R.M. Stanciuc, R. Bimbasa 12

PROPULSION, SPACE

- Development of a Transport and Storage Container for a Space Optical Instrument
I.F. Popa, D. Mihai, G. Megherelu, R. Mihalache, E. Nutu 21

MATERIALS AND TECHNOLOGIES

- Comparison of Different Additive Manufacturing Methods for Pre-evaluation of Centrifugal Pump Components
I.F. Popa, D. Mihai, M. Vladut, D. Asoltanei 35

- Computational and experimental Study on Defect Emergence in Investment Cast Compressor Blade for Industrial Gas Turbine
M.R. Condruz, T.A. Badea, T.F. Frigioescu, A. Paraschiv, C. Todea 43

Editorial

O Fresca Florentina in Pandemie

Afirmația că de peste un an și jumătate realitatea lumii noastre s-a schimbat dramatic este deja un truism. Conștienți de pericolele care ne pândesc la nivel global și la nivel personal, stăruința de a ne proteja și de a proteja devine dominantă. Și totuși, dincolo de această primă necesitate există ceva care ne definește: *aspirațiile*.

Ne punem întrebări legate de rezistență, căutăm repere istorice și repere de comportament printr-o prismă temporală, pentru a ne concretiza aceste aspirații. Ne putem opri în secolul XIV, într-un an al *Renașterii*, 1348, aflat sub dominația catastrofală a ciumei asupra întregii Europe, să urmărim întâlnirea a zece tineri, șapte fete între 18 și 28 de ani și trei băieți de 25 de ani, în biserica Santa Maria Novela din Florența. Teroarea omniprezentă face ca dragostea de viață a acestora să prevaleze și întregul grup să propună retragerea la țară, într-un decor idilic, pentru două săptămâni, ca formă de rezistență și de celebrare a vieții. Pentru această retragere tinerii își vor impune propriile reguli: zilnic fiecare va spune zece povești, cu excepția zilelor unu și nouă alocate devoțiunii religioase și îngrijirii; zilnic vor fi bine dispuși, se vor bucura de natură, iar fiecare dintre cei zece va fi „rege" sau „regină" pentru o zi, purtând o cunună de lauri, suveranul fiecărei zilei fiind și cel ce dă tema poveștilor. Libertatea de a-și petrece ceasurile de răgaz după bunul plac mai are totuși o impunere, explicabilă pentru regula deconectării: în perimetrul refugiului lor să nu ajungă decât veștile bune din afară.

Aceasta este tema *Decameronului* lui Giovanni Boccaccio, ce a cartografiat admirabil contextul cultural și social al vremii, fapt care-l exonerează de imputările privind frivolitatea unor pasaje. Boccaccio și-a ales exponenții frumoși, tineri, spirituali, de nădejde, respectând regulile convenției epice impuse chiar de ei, refugiul făcându-i să uite de realitatea amenințătoare a epidemiei de ciumă și să se simtă protejați și mai cu seamă prolifici și plini de viață. Cele o sută de povești spuse de zece personaje sănătoase și educate, vreme de zece zile, sunt în opoziție cu teribila boală, conțin glume, ironii, istorii de dragoste mai mult sau mai puțin fericite sau parabole filozofice. Autorul face din epidemie un simbol al obscurantismului, fricii și morții și conturează filonul filozofic pe contrastul viață (tinerii eroi) - moarte (ciuma). Cum în *Renaștere* antropocentrismul a cunoscut gloria, *Decameronul* va confirma potrivit epocii, calitățile umane: inteligență, generozitate, frumusețe, spirit și educație.

Decameronul lui Giovanni Boccacio a fost inclus în anul 1559 în Indexul cărților interzise, lucru ce nu i-a împiedicat circulația pe ascuns. Timpul însă i-a conferit, tocmai datorită antropocentrismului relevat, un titlu nou: *Comedia umană*, iar pe lângă *Divina Comedie* a lui Dante, lucrare a *Renașterii* timpurii (care își datorează atributul divina tocmai lui Boccacio ca autor al biografiei lui Dante, acesta numind-o simplu *Commedia*), astăzi ne putem bucura și de această lucrare vie a *Renașterii*.

Nenumărate întrebări trebuie să-i fi copleșit pe cei zece tineri la sfârșitul experimentului, însă forța și persistența acelor întrebări i-a provocat și i-a obligat pe mai departe să reexamineze contextul vieții și epocii lor, pentru că înțelegerea vine doar atunci când acest context este provocator și impune reconsiderări. Lectura acestui decameron este pretext pentru a înțelege astăzi că și alți oameni, în alte epoci, au luptat la fel, au construit lucruri care în prezentul lor nu au putut fi cuantificate, dar cu siguranță s-au conturat peste o generație sau mai multe.

Ec. Elena Banea,
Decembrie 2021

Editorial

A Florentine Fresco in Full Pandemic

The claim that the reality of our world has changed dramatically over a year and a half is already a truism. Aware of the dangers that await us on both global and personal scales, perseverance to protect and protect ourselves becomes dominant. And yet, beyond this first need, something defines us: *aspirations*. We ask ourselves questions related to endurance, we look for historical landmarks and landmarks of behavior from a temporal perspective, to make these aspirations come true.

We can make a halt back in the 14th century, during the *Renaissance*, in 1348, for example, a year catastrophically dominated by the plague all over Europe, watch the meeting of ten young people, seven girls between 18 and 28 years old and three boys of 25 years old, in the church of Santa Maria Novela in Florence. The ubiquitous terror makes their love of life prevail; therefore, the whole group decides to retreat in the countryside, in an idyllic setting, for two weeks, as a form of resistance and celebration of life. During their retreat, young people will settle their own rules: each will tell ten stories daily, except for day one and nine that will be dedicated to religious devotion and care; they will be always in a good mood, enjoy nature and each of them will be "king" or "queen" for a day, wearing a laurel wreath, the sovereign of each day being the one who provides the theme of the stories. Yet, the freedom to spend their leisure hours at their own will have an imposition, explainable by the rule of detachment: only good news from the outside to reach the perimeter of their shelter.

This is the theme of Giovanni Boccaccio's *The Decameron*, which admirably mapped the cultural and social context of the time, an aspect that exonerate him from the accusations regarding the frivolity of some of his passages. Boccaccio chose his beautiful, young, spiritual, trustworthy exponents by respecting the rules of the epic convention imposed by the characters themselves. The refuge makes them forget the threatening reality of the plague epidemic and feel protected and, especially, prolific and full of life. One hundred stories told by these ten healthy and educated characters during the ten days are in contrast with the reality of the terrible disease; these stories contain jokes, a lot of irony, more or less happy love stories or philosophical parables. The author defines the epidemic as a symbol of obscurantism, fear and death, and he outlines the philosophical vein based on the contrast between life (young heroes) - death (plague). As anthropocentrism knew its glory during the Renaissance, *The Decameron* confirmed certain human qualities, such as intelligence, generosity, beauty, spirit and education, according to the trend of those times. In 1559, Giovanni Boccacio's *The Decameron* was included in the Index of Prohibited Books, but did not prevent it from circulating secretly. In time, however, its title changed into *The Human Comedy*, precisely due to its revealed anthropocentrism, in addition to Dante's *Divine Comedy*, an early Renaissance work (which owes its 'divine' attribute to Boccacio himself, as author of Dante's biography, which he simply called *Commedia*), today we can enjoy this lively work of the *Renaissance* as well.

Countless questions must have overwhelmed those ten young people at the end of the experiment, but the strength and persistence of those questions challenged and forced them to reexamine the context of their lives and times because understanding comes only when the context is challenging and asks for reconsideration. Reading this decameron is a pretext to understand today that other people too fought the same way, yet in different eras, built things that could not be quantified during their times, but which certainly took shape over at least one generation later.

Ec. Elena Banea,
December 2021

PASSENGERS MONITORING SYSTEM WITH INFRARED SENSORS AND MICROCONTROLLER

Daniel LALE[1], Claudia BORZEA[1,2], Sorina GOGONEAȚĂ[2], Cristian NECHIFOR[1,2], Mirela VASILE[1,2], Filip NICULESCU[1]

Received: 14.06.2021
Accepted: 06.07.2021
Published: 20.12.2021

Copyright: The article is an Open Access article and it is distributed under the terms and conditions Creative Commons Attribution (CC BY) license (**https://creativecommons.org/licenses/by/4.0/**).

ABSTRACT: The paper presents a system for counting and monitoring passengers in public transportations means, such as buses and subway trains, where crowding is an inevitable issue. The urban agglomerations have been recorded even in the last two years, when physical distancing has been continuously encouraged. However, this becomes almost impossible in everyday life when people have to get to the workplace via public transportation. The system proposed uses infrared sensors for counting passengers getting up and down a public vehicle. The infrared sensors can be used both for detection, as well as for measuring the temperature, providing a temperature map. Thresholds can be set for temperatures exceeding certain limits, and an alarm signal can be given when a person with fever has passed through the sensing range of the sensors placed on the upper part of the doors. Microcontrollers are proposed for the monitoring system, both in the central processing unit, as well as in the local processing units.

KEYWORDS: Infrared Sensors, Passengers Counting, Public Transport, Temperature Monitoring, Microcontroller, Piezoelectric Quartz Resonator

NOMENCLATURE
BLOB – Binary Large OBject;
CPU – Central Processing Unit;
GSM – Global System for Mobile Communications;
I^2C – Inter-Integrated Circuit;
IR – Infrared;
LPU – Local Processing Unit;
PWM – Pulse Width Modulation;
RAM – Random Access Memory;
RF – RadioFrequency;
SARS-CoV-2 – Severe Acute Respiratory Syndrome CoronaVirus 2;
SPI – Serial Peripheral Interface;
UART – Universal Asynchronous Receiver/Transmitter.

1. INTRODUCTION

An increased research interest towards automated passengers monitoring system has been recorded over the last few years. Intelligent transportation systems are developing at a rapid pace and are being integrated with automated systems for managing passengers throughput [1]. A reliable monitoring system [2] can provide a valuable data archive in public vehicles regarding passengers number, vehicle tracking and other such

[1] Romanian Research and Development Institute for Gas Turbines COMOTI, Automation and Electrical Engineering Department.
[2] Doctoral School of Electrical Engineering, University Politehnica of Bucharest.

information that can prove to be very useful in assessing various operational elements and parameters, including solving customer complaints. The system can also be implemented as a protection measure for stopping the spread of viruses making body temperature rise, for the early isolation of a person who exceeds a body temperature threshold, before this one gets into the public vehicle and possibly infects others.

There are various types of systems for passenger counting, some using infrared sensors [3-5] within the sensor barriers at the entrances to public transport vehicle, thermal sensors, Wi-Fi based [6] etc. The most commonly encountered system is still the one using video cameras and image processing [7-8]. The main disadvantage of the visual counting system is the cost and, even with high-resolution cameras, the system has high inaccuracies. For example, if a person wears the same shades of grey as in the rooms' background set for counting, it will be difficult to distinguish the person wearing grey clothing. So, one of the most accessible passengers counting devices are infrared beam sensors that work on the principle that all objects emit heat in the form of electromagnetic radiation, with a certain wavelength which depends on the temperature increase of the radiant object and its spectral emissions. Fig. 1 presents a counting system with IR sensors and cameras.

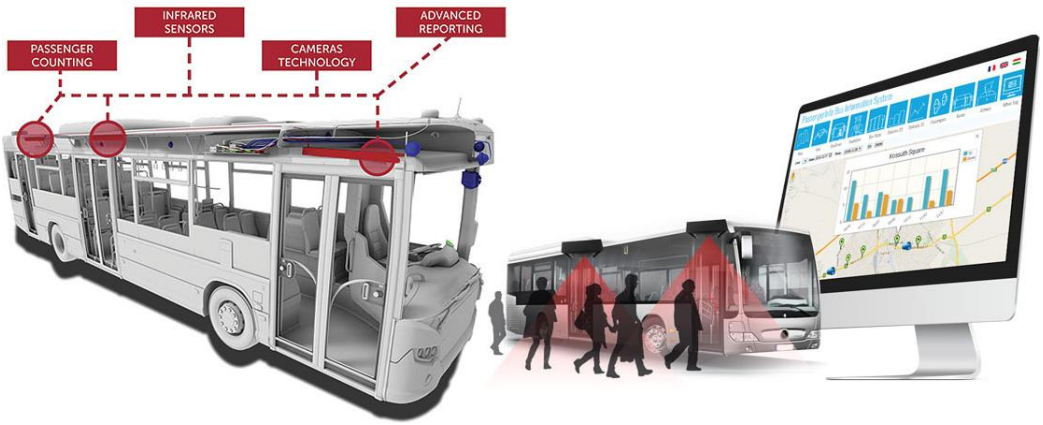

Fig. 1. Bus monitoring system with infrared sensors and video cameras [9]

The paper herein proposes a design solution for monitoring both the number and body temperature of the passengers, reducing equipment costs and simplifying implementation works required. Using IR sensors, the system can provide real-time data on the number of passengers, occupancy rate of the vehicle and can track vehicle's position, along with monitoring body temperature.

Avoiding crowds and monitoring temperature represents a measure that has been recommended and even enforced during the spread of SARS-CoV-2 virus, starting to be perceived as a very serious at global level beginning from early 2019, with certain restrictions still continuing up to present date. An increased awareness regarding infectious diseases spreading in public agglomerations has been recently recorded [10].

2. THE PROPOSED SYSTEM

Passenger monitoring and counting can be performed by a system using infrared sensors, in a configuration like the proposed block diagram in Fig. 2 below.

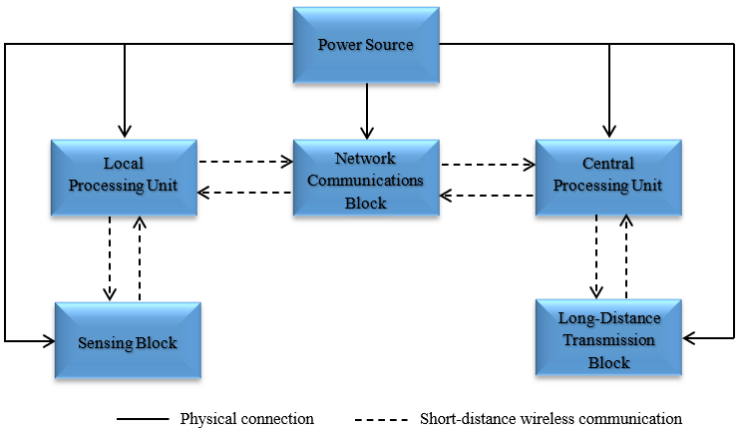

Fig. 2. Block diagram of the counting system

The central processing unit is connected to the local processing units, acting as a managing unit for the data received from these ones. The CPU updates the occupancy of the public transport vehicle and sends the updated data to the control centre, by means of the long-distance transmission block. The occupancy rate is updated by adding or subtracting the number of passengers getting up or down the vehicle, to their current number. Following this procedure, the updated data shall be transmitted to the command centre.

The central processing unit includes:

- **Microcontroller (ATMega328P-PU)**, high-performance and capable of executing internally up to 16 million instructions per second. UART, I^2C and SPI communication protocols can be used for data transmission. Unlike SPI and I^2C, UART is actually not a communication protocol as per, but a physical circuit integrated in a microcontroller, or a stand-alone IC. The main purpose of UART is to transmit and receive serial data [11].

  This microcontroller is one of the most popular and reliable for many applications, such as in robotics, easing the sensors programming for all sorts of low power applications, via Arduino development boards. The ATMega328P in DIP (Dual In-Line Package) format [12] comes without a boot loader, which can be programmed with another Arduino. For making this chip capable of working in stand-alone mode, a 16 MHz oscillator or resonator and a 5 V power supply have to be connected.

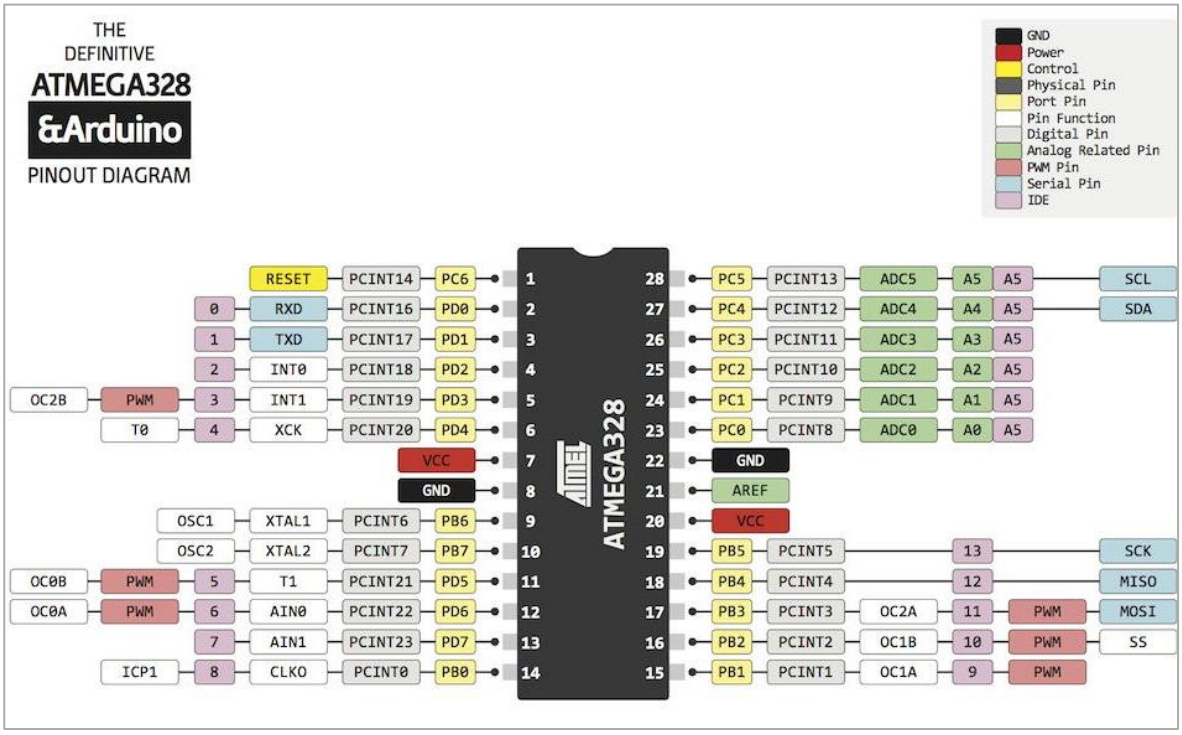

Fig. 3. Microcontroller pinout diagram [12]

- **A 16 MHz quartz crystal resonator** with the main function of generating a stable electrical signal of a certain frequency, used to synchronize all the internal operations of the microcontroller in order to obtain a higher processing speed. Crystal oscillators use a mechanically resonant circuit based on a piezoelectric element, for the feedback loop of an amplifier, usually made of a quartz crystal. The size (thickness in our case) of piezoelectric materials changes when applying an alternating electric field across two faces (inverse piezoelectric effect). Similarly, an electric charge is generated when the material is deformed by an applied force (direct piezoelectric effect).

  The resonant frequency of the crystal maintains a high stability because it is primarily determined by the physical size. Since the size of the crystal is a function of its temperature, the frequency may change with temperature. However, in crystals of certain orientations (cuts), these fluctuations of the piezoelectric response with temperature can be reduced and considered to be negligible in high precision applications (sub-nanometre order). Piezoelectric crystals are available in a range of standard resonant frequencies between 10 kHz to 100 MHz [13].
- **Two ceramic capacitors** of 18 pF capacitance, for the stabilization of the oscillator's resonant frequency, according to manufacturer recommendations regarding resonator's load capacitance [14].
- **A 10 kΩ resistor** is introduced in the circuit, for preventing any accidental resets of the microcontroller. The resistor value is 1/10 of the internal microcontroller's resistance (100 kΩ). This pull-up resistor on the reset pin is used together with a switch, with the role of limiting the current to the reset pin, keeping

this one continuously power supplied. Digital logic circuits have three logic states: high, low and floating (or high impedance). The high-impedance state occurs when the pin is not pulled to a high or low logic level, being left floating. The microcontroller might unpredictably interpret the input value as either of them, causing a false green LED to light up on the pin that can also be affected by radiated environmental energy [15]. Without the resistor, the button would connect V_{CC} to ground, causing a short-circuit [16].

The components in Table 1 are necessary for the bootloader installation. The bootloader is a program running in the microcontroller enabling this one's programming. When a new program is loaded, the bootloader takes over the data and writes it to the microcontroller's memory.

Table 1. Components used for bootloader installation within the central processing unit

No.	Component	Value [UM]	Characteristics / operating principle / role	Type
1.	**Microcontroller**	8 b data bus width, at frequency of 20 MHz	DIP format, 1.8 V ÷ 5.5 V voltage supply, 32 kB flash memory, 2 kB RAM 23 programmable I/O (Inputs/Outputs), 6 PWM channels	ATMega328P
2.	**Resonator**	16 MHz (resonant frequency)	Quartz crystal sandwiched between two metallic electrodes / Based on inverse piezoelectric effect	ECS-160-18-4X-CKM
3.	**Capacitors**	18 pF (capacitance)	Ceramic capacitor	D180G20C0GH63L2R
4.	**Resistor**	10 kΩ (electrical resistance)	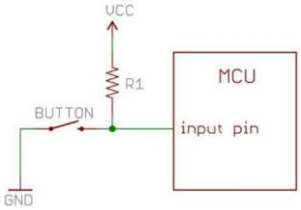 Short-circuit prevention [16]	MF01SFF1002A10

The CPU communicates with the local processing units, and with the command and control centre respectively, by means of the GSM module (Fig. 4) and transceiver module (Fig. 5).

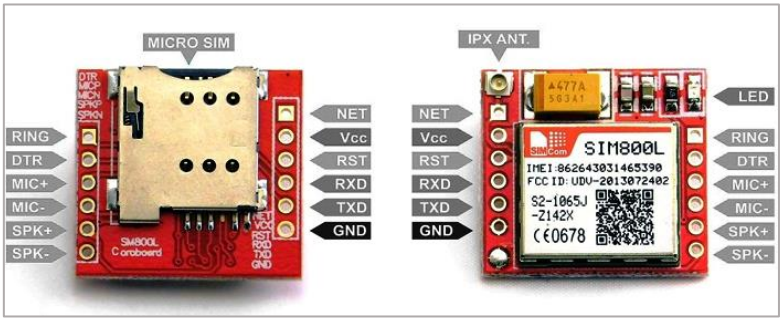

Fig. 4. Pinout diagram of the GSM module [17]

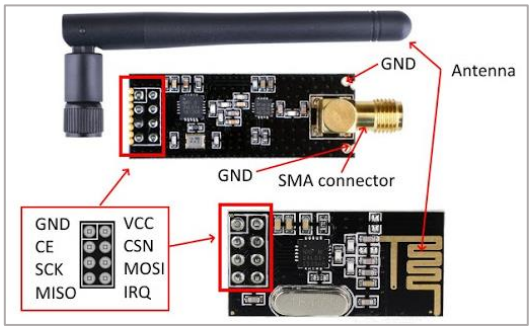

Fig. 5. Pinout diagram of the transceiver module [18]

1. **GSM SIM800L module** – a block for data transmission over long distances, and practically a module that operates on four frequency bands using a SIM card for data exchanges with the command centre. The module is connected to the CPU via the UART serial connection. The CPU microcontroller uses a 5V logic level (1 logic), while the GSM module uses a 2.8V logic level (1 logic), therefore a level converter is required for realising the data exchange between the two units.
2. **nRF24L01 radio module –** a transceiver (transmitter/receiver) operating in 2400 MHz to 2450 MHz frequency band. This specific frequency band is an unlicensed frequency band suited for transmissions without any legal constraints. The transceiver can transmit on 125 channels, but for our applications, only the last 25 channels are used, since they generally have a higher frequency than Wi-Fi routers, thus reducing the electromagnetic noise and perturbations in the transmission medium. A frequency is assigned for each channel, according to relation (1) hereinafter.

$$f_{radio} = f_{low} + f_{ch} \tag{1}$$

where: f_{radio} [MHz] – transmission radiofrequency; f_{low} = 2400 MHz – lower bandwidth frequency; f_{ch} [MHz] – channel frequency value (added).

Each channel of the module comprises six parallel sub-channels. Each sub-channel is allocated its own address that can be configured separately. Practically, the module set as main receiver simultaneously collects information from six different transmitters. Thus, a tree topology can be realised, the base being the CPU, while the nodes are represented by the LPUs of the public transport vehicle.

The local processing unit performs data exchange with the central processing unit and consists of the same components as the main unit: the ATMega328P-PU microcontroller, a 16 MHz quartz crystal oscillator, two 18 pF ceramic capacitors and a 10 kΩ resistor for enabling the loading of the Arduino code. This unit has monitoring function, counting the passengers by analysing the data collected from MLX90640 infrared sensor representing the sensing unit or block in the diagram in Fig. 2.

The infrared sensors principle of operation, depicted in Fig. 6 below, is based on the principle that all objects emit radiation with a certain a wavelength within the infrared region of the electromagnetic radiation spectrum. Infrared radiation is also known as thermal radiation, since it is mainly generated by heat.

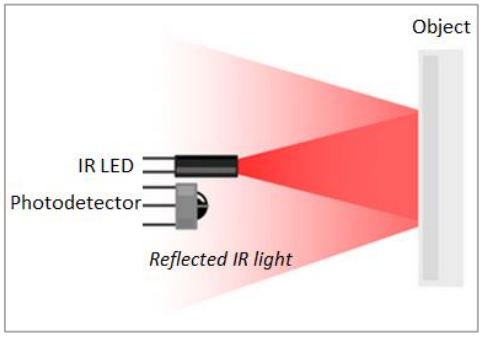

Fig. 6. Infrared sensors operation principle [19]

The MLX90640 [20] is an infrared sensor with thermopiles, consisting of several thermocouples connected in series or in parallel. This IR sensor has a fast response and ability to adapt the measurements

according to the ambient temperature. The integration of thermopiles enables the measurement of the objects' temperature, by measuring the radiation intensity, and can also generate a 768 pixels infrared thermal image.

3. DETECTION AND COUNTING ALGORITHM

In order to determine the number of moving passengers, the frame difference technique is used, which memorizes the first pixels frame at system start up, when no passenger is found within the detection area. If the IR sensor detects a moving person, the LPU compares the stored pixel frame with the pixel frame when the motion was detected. Thus, the local processing unit realises a background subtraction, and only the pixels of interest are maintained, which are associated with a so-called binary large object (BLOB).

Tracking an object can be categorized as an event, so if more objects are detected in the current frame than in the previous one, a new event is created. The identification of the event with a certain object is realised subsequently, after data processing by the microcontroller. If the number of objects from the current and previous frames is the same, then a one-to-one mapping is established between the objects in those frames, and the object tracking is resumed. The tracking of an object from previous frame is continued in the current frame with its thermal footprint associated. The association is made according to Euclidean distance between the centroids of the objects. The Euclidean distance between two points found in a Euclidean space is the length of the segment connecting the two points. This one can be determined relying on these points' Cartesian coordinates, applying Pythagoras's theorem. The Euclidean distance can be calculated with relation (2):

$$d(x,y) = \sqrt{\sum_{i=1}^{n}(y_i + x_i)^2} \quad \textbf{(2)}$$

where: x, y – points in Euclidean space; y_i , x_i – Euclidean vectors (starting from initial point considered in the origin of the Euclidean space; n – n-dimensional Euclidean space.

First of all, for each object in the current frame, the closest object from the previous frame is determined. Then, the objects with the smallest Euclidean distance between their centroids are associated with one another. The procedure is repeated iterating for the current frame with the next one and so on. If fewer objects are found in the current frame than in the previous one, the algorithm stops tracking the object, as it it is no longer present in current frame (Fig. 7). This method is applied for compensating the sensor's low resolution, short time during events, as well as due to similarities between thermal spectrums of different people. When the tracking of an object is completed, an IN (inside) or OUT (outside) value is assigned to the object, by analysing the pixels' motion direction, coloured depending on the object's temperature.

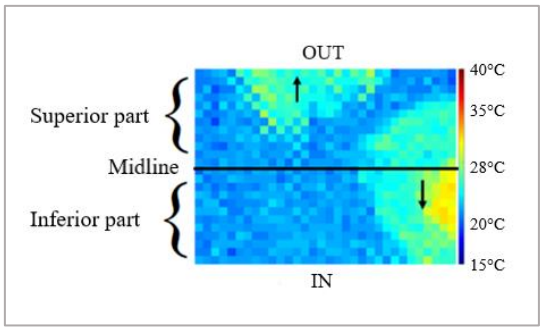

Fig. 7. Thermal pixels frame outlining inside and outside objects trajectories

The centroid consists of horizontal components (C_n^h) and vertical components (C_n^v). The centroid position is determined with relation (3) hereinafter.

$$C_t = \frac{1}{|F_t|}\sum_{x \in F_t} x \quad \textbf{(3)}$$

where: x, y – points in Euclidean space; C_t – Centroid at t moment; F_t – Pixels set of one object at t moment.

Since the columns in a thermal frame are normal to the vehicle door, the vertical components of the centroid (C_n^v) are used to verify whether a person is getting on or off the vehicle, checking if the centroid

crosses or not the midline of the frame between two moments of time *t-1* and *t*. If the vertical component of the centroid is on inferior part of the frame (inside vehicle) at *t* moment, and at *t-1* it is on the superior part (outside vehicle), it is considered that the passenger is no longer inside the vehicle (see Fig. 7 above). With this algorithm, the data is transmitted to the CPU, which updates the passengers' number.

Fig. 8 presents the breadboard implementation [21] of the components used for designing the central processing unit. Breadboards are designed for electronic circuits prototyping, easing the implementation of through-hole electronic components, without the need of permanent soldering to a printed circuit board. If the practical implementation is desired, the conceptual prototype presented shall be realised according to PCB standards for the given applications, by contracting a specialised company [22]. A LM7805 voltage regulator with higher input voltage was also introduced in the circuit, ensuring a stable 5 V supply.

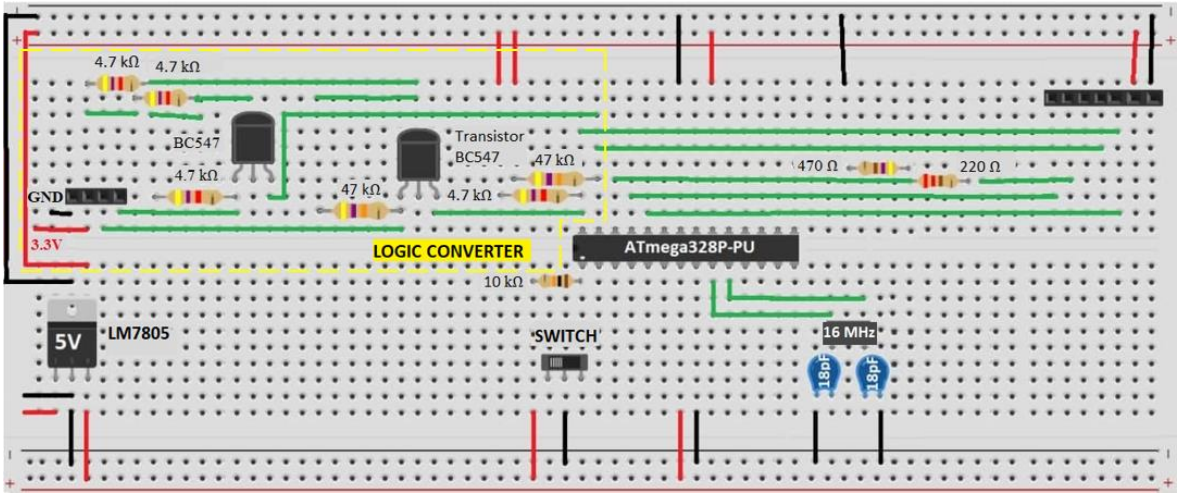

Fig. 8. Breadboard implementation of central processing unit components

4. CONCLUSIONS

Due to an unorganised public transport system and overcrowded vehicles specially at rush hours occurring in the morning and afternoon during workdays, the number of personal vehicles has risen. These ones represent a major factor for increasing pollution and traffic jams.

While much cleaner air was recorded during the lockdown, it is safe to conclude that reducing the personal vehicles number would contribute to the planet's regeneration in terms of reducing the emissions from partially burnt gases. The paper proposes a solution for reducing pollution factors, by counting the passengers. By analysing the data, it can be established which routes and segments are overly used (underestimated) and which ones are less used. This way, it can be estimated on which lines to increase or reduce the number of vehicles, and the time intervals when there should be a more frequent public transport traffic. The routes can also be reorganised, minimising the usage of each vehicle or line. A public transport fluidisation and optimisation would increase its usage in the detriment of personal vehicles.

Comparing to other systems for counting passengers, which have a high implementation and starting costs, the proposed system is a very cost-effective solution and easy to implement, both regarding the reduced costs of the components, as well as in terms of efficiency for data processing. Using infrared sensors maintains the identity of the passengers confidential. Another advantage of a monitoring system with infrared sensors is the possibility to hinder persons with fever from getting on the vehicle, by setting temperature thresholds.

A future improvement that can be brought to the system proposed would be introducing video cameras, which would help detect the specific person who has to be quarantined. It would also be a measure for reducing the crime rate (such as thefts, harassments, etc.) and increasing the response in case of emergencies or unexpected events.

REFERENCES

[1] R. Sutopo, J. Lim, V. Baskaran, K. Wong, M. Tistarelli and H. Liau, "Appearance-based passenger counting in cluttered scenes with lateral movement compensation", *Neural Computing and Applications*, 2021. DOI: 10.1007/s00521-021-05760-x

[2] A. Olivo, G. Maternini and B. Barabino, "Empirical Study on the Accuracy and Precision of Automatic Passenger Counting in European Bus Services", *The Open Transportation Journal*, vol. 13, no. 1, pp. 250-260, 2019. DOI: 10.2174/1874447801913010250.

[3] D. Klauser, G. Bärwolff and H. Schwandt, "A TOF-based automatic passenger counting approach in public transportation systems", 2015. DOI: 10.1063/1.4913168.

[4] C. Kuenzer and S. Dech, *Thermal Infrared Remote Sensing: Sensors*. Dordrecht: Springer Netherlands, 2013. ISBN 978-94-007-6639-6.

[5] "Automatic Passenger Counting System for buses | Land Transport Guru", *Land Transport Guru*, 2021. https://landtransportguru.net/automatic-passenger-counting-system/.

[6] M. Nitti, F. Pinna, L. Pintor, V. Pilloni and B. Barabino, "iABACUS: A Wi-Fi-Based Automatic Bus Passenger Counting System", *Energies*, vol. 13, no. 6, p. 1446, 2020. DOI: 10.3390/en13061446.

[7] F. Li, F. Yang, H. Liang and W. Yang, "Automatic Passenger Counting System for Bus Based on RGB-D Video", *Proceedings of the 2nd Annual International Conference on Electronics, Electrical Engineering and Information Science (EEEIS 2016)*, 2017. DOI: 10.2991/eeeis-16.2017.29.

[8] D. Liciotti, A. Cenci, E. Frontoni, A. Mancini and P. Zingaretti, "An Intelligent RGB-D Video System for Bus Passenger Counting", *Intelligent Autonomous Systems 14*, pp. 473-484, 2017. DOI: 10.1007/978-3-319-48036-7_34.

[9] "Bus Passengers Counting Product & Integration Solution", *Smartcomm.biz*, 2021. https://www.smartcomm.biz/bus-passengers-counting-product-integration-solution/.

[10] P. Kumar, A. Khani, E. Lind and J. Levin, "Estimation and Mitigation of Epidemic Risk on a Public Transit Route using Automatic Passenger Count Data", *Transportation Research Record: Journal of the Transportation Research Board*, p. 036119812098513, 2021. DOI: 10.1177/0361198120985133.

[11] "UART vs I2C vs SPI – Communication Protocols and Uses - Latest open tech from seeed studio", *Latest open tech from seeed studio*, 2021. https://www.seeedstudio.com/blog/2019/09/25/uart-vs-i2c-vs-spi-communication-protocols-and-uses/.

[12] "Atmega328P-PU DIP-28 - Opencircuit", *Opencircuit*, 2021. https://opencircuit.shop/Product/Atmega328P-PU-DIP-28.

[13] D. Crecraft and S. Gergely, "Signal generation", in *Analog Electronics*, pp. 263-281, 2002. DOI: 10.1016/B978-075065095-3/50011-8.

[14] "ECS-160-18-4X-CKM – Mouser Romania", *Ro.mouser.com*, 2021. https://ro.mouser.com/ProductDetail/ECS/ECS-160-18-4X-CKM?qs=7MVldsJ5UawYqyimirccKw%3D%3D&utm_source=eciaauthorized&utm_medium=aggregator&utm_campaign=ECS-160-18-4X-CKM&utm_term=ECS-160-18-4X-CKM&utm_content=ECS.

[15] EE Power, "Pull up resistor / Pull down resistor. Chapter 5 - Resistor applications", *eepower.com*, 2021. https://eepower.com/resistor-guide/resistor-applications/pull-up-resistor-pull-down-resistor/#.

[16] "Pull-up Resistors - learn.sparkfun.com", *Learn.sparkfun.com*, 2021. https://learn.sparkfun.com/tutorials/pull-up-resistors/all.

[17] U. Arduino and G. Electronics, "SIM800L & SIM800L EVB v2.0 - Variations and wiring", *Arduino Forum*, 2021. https://forum.arduino.cc/t/sim800l-sim800l-evb-v2-0-variations-and-wiring/505185.

[18] "ACES: ICS3U", *Darcy.rsgc.on.ca*, 2021. http://darcy.rsgc.on.ca/ACES/TEI3M/2021/Content.html.

[19] A. Pluess, "PrintTest", *Aplu.ch*, 2021. http://www.aplu.ch/home/printcenter.jsp?center_to_include=microbit_ex7.html.

[20] Y. Wu, H. Liu, B. Li and R. Kosonen, "Prediction of thermal sensation using low-cost infrared array sensors monitoring system", *IOP Conference Series: Materials Science and Engineering*, vol. 609, p. 032002, 2019. DOI: 10.1088/1757-899X/609/3/032002.

[21] "Tinkercad | From mind to design in minutes", *Tinkercad*, 2021. https://www.tinkercad.com/.

[22] "The Ultimate Guide to PCB hardware | Global Manufacturer & Distributor of Component Solutions — Essentra Components", *Essentracomponents.com*, 2021. https://www.essentracomponents.com/en-gb/news/guides/the-ultimate-guide-to-pcb-hardware.

COUPLING TORSIONAL VIBRATION ANALYSIS OF A SCREW COMPRESSOR - CATERPILLAR ENGINE SYSTEM

Iulian VLADUCA[1], Radu IONESCU[1], Carmen Gheorghita PETRE[1], Ramona Manuela STANCIUC[1], Razvan BIMBASA[1]

Received: 06.08.2021
Accepted: 16.11.2021
Published: 20.12.2021

Copyright: The article is an Open Access article and it is distributed under the terms and conditions Creative Commons Attribution (CC BY) license (**https://creativecommons.org/licenses/by/4.0/**).

ABSTRACT: The present paper details a torsion study for coupling between a screw compressor and a Caterpillar engine, with the aim of determining the torsional vibrations that may occur in the shaft during the operation of the compressor on the entire range of speeds and loads to avoid the resonance phenomenon. The shaft system is consisting in the Caterpillar engine crankshaft, flywheel, coupling and screw compressor and the study is necessary to find the dangerous frequencies during operating modes. To determine the free torsional vibrations that occur in the shaft line of the two machines coupled by an elastic coupling, an equivalent oscillating system of the shaft line with the Holzer method was taken into account.

KEYWORDS: CU screw compressor, Caterpillar engine, free torsional vibrations, Holzer method

NOMENCLATURE

θ [rad] - angular deformation.
G [N/m^2] - shear modulus
I_p [m^4] - polar moment of inertia of its section
M_t [Nm] - torque
L [m] - the distance between two cross sections
Θ [rad] - amplitude
ω [rad/s] - pulsation
K_j [Nm/rad]- torsional stiffness of equivalent j shaft sections
J [Nms^2] - polar mass moment of inertia
d_e [m] - equivalent shaft diameter
l_{ej} [m] - equivalent length of the shaft section number j.

1. INTRODUCTION

The work started with the study of replacing electrical motors with internal combustion engines, in this case a Caterpillar 3304G, in driving screw compressors intended for methane gas, to ensure the autonomous operation of these groups, in areas without electricity mains access. The main objective of replacing the electrical motor with a thermal engine, is because that the fuel used to run the ICE is the same gas that is compressed, and electrical power is not necessary in the working area. In the real world, many wells operate in isolated areas with difficulties regarding facilities for equipment operation, including insufficient power supply.

[1] Romanian Research and Development Institute for Gas Turbines COMOTI

The solution being to drive the compressors with thermal engines, usually piston engines, powered by natural gas obtained directly from the wells. Many small companies, are interested in technologies and equipment for depleted gas wells exploitation.

The use of such technologies and equipment is based on the need for optimal use of the country's crude oil and natural gas resources and on the national effort to provide material and energy resources, as a basis for sustainable development of the economy under the use of environmentally friendly technologies and equipment.

In collaboration with the beneficiaries from Romania and abroad, research and development programs have been started to increase the performance and reliability of gas compressors. Based on the experience gained, COMOTI has channelled its research into compression groups consisting of screw compressors and natural gas fuelled ICEs, for placement in the gas field, near wells, including depleted ones.

The use of screw compressors allows almost complete extraction of gases from depleted deposits, because this type of compressor has the ability to operate at pressures close to zero relative and even with negative pressures, achieving high compression ratios in one stage.

2. STUDIED EQUIPMENT AND THEORETICAL CONSIDERATIONS

For the study of the own vibrations of the thermal engine - coupling - screw compressor, the MCS 15.6 motor compressor [1] was used as a test bed, being equipped with Caterpillar 3304G thermal engine [2], of 71 kW, and CU90G [3] screw compressor, see figure 1 below:

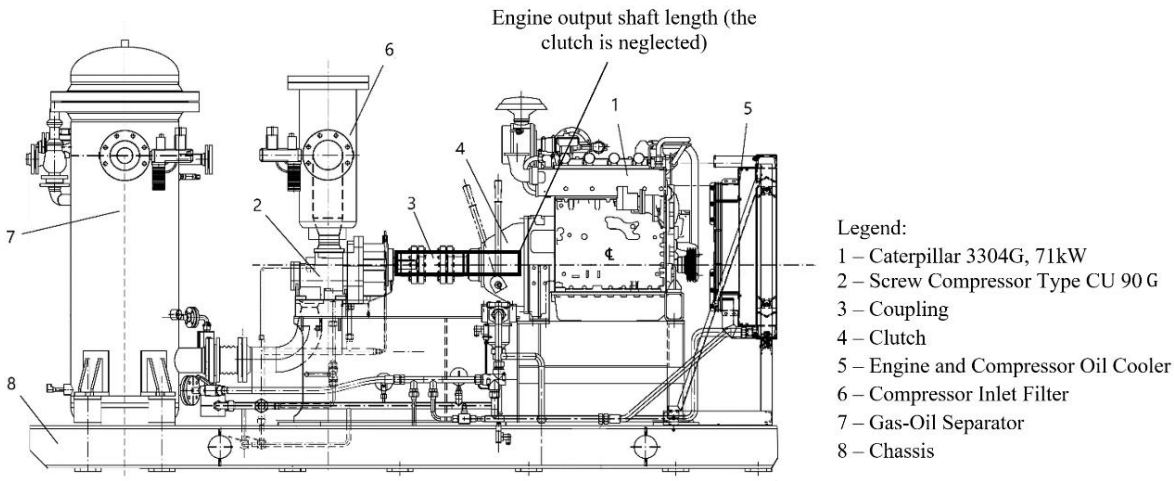

Fig. 1. Compressor assembly, equipped with Caterpillar 3304G engine and CU90G screw compressor

The first project study [1] of compressing natural gas using a screw compressor driven by a natural gas fuelled ICE, was designed to use a CF family type screw compressor produced by GHH - Ingersol Rand, the actual test bed, replaced the no longer in production CF type compressor unit, with a newer one, from CU type that is produced by the National Research and Development Institute for Gas Turbines COMOTI, under a GHH-Ingersol Rand license [3, 4].

The CU screw compressor series were specially developed for application in refrigeration, air-conditioning and heatpump installations and consists of three initial models: CU64G, CU90G, and CU128G. Under the mentioned GHH license and with an ATEX certification [5] given by INSEMEX, Petroşani from Romania, the CU series were adapted for work in areas with potentially explosive atmosphere, certification zone II, category 3 equipment.

The CU 90G compressor performances are presented in the figure 2 below [3].

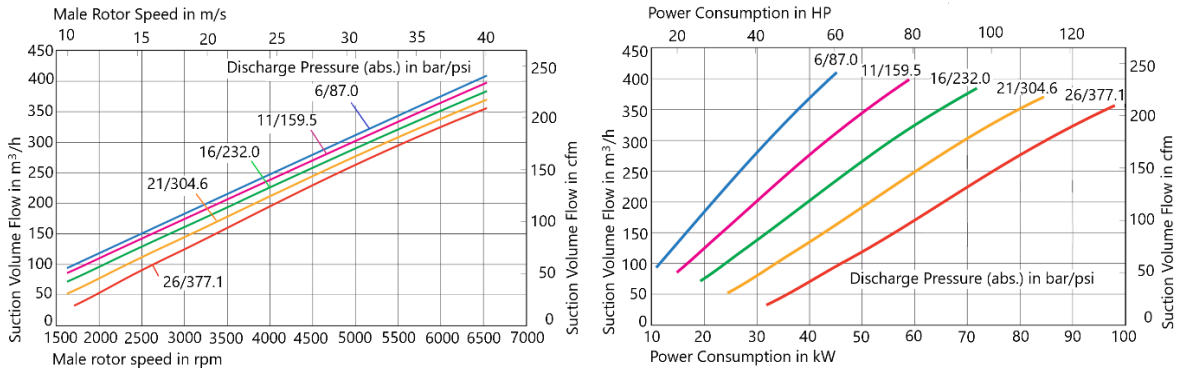

Fig. 2. Compressor CU 90G performances

The compressor performances were presented to indicate the maximum rotational speed of the male rotor for all driver rotational speeds, from 1450 to 3550 rpm as also indicated in the CU compressor manual. A special feature of the CU compressors, is the integrated gearbox. This allows adjustment of the compressor speed, whithin the range of the allowable male rotor speeds, and thus of the suction volume to match the service conditions. In a case of a frequency controlled electric driver, a continuous fine tuning of the speed with the current operating conditions may be done. In the present work, the driver is a termical Caterpillar 3304G (G – for gas) engine [6], with an operational working speed of 1800 rpm. The compressor unit is connected with the Caterpillar engine with a cluch, position 4 in the legend, see the figure 1 above, when the nominal speed is achieved. The Caterpillar 3304G can vary continuously his speed up 75% down from the nominal speed, to about 1350 rpm, by a gas - pressure regulator [7]. The system screw compressor - Caterpillar engine can cover the entire range of working speed of the compressor unit CU 90G, to the limits of the engine.

In the figure 3 are shown the main parameters of the Caterpillar 3304G:

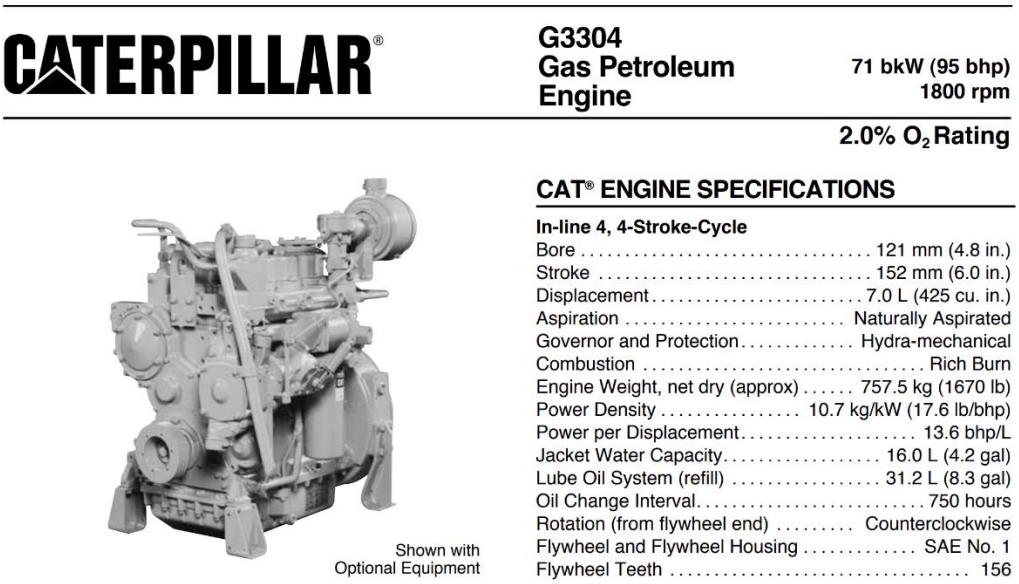

CATERPILLAR®

G3304
Gas Petroleum
Engine

71 bkW (95 bhp)
1800 rpm

2.0% O_2 Rating

Shown with
Optional Equipment

CAT® ENGINE SPECIFICATIONS

In-line 4, 4-Stroke-Cycle

Bore	121 mm (4.8 in.)
Stroke	152 mm (6.0 in.)
Displacement	7.0 L (425 cu. in.)
Aspiration	Naturally Aspirated
Governor and Protection	Hydra-mechanical
Combustion	Rich Burn
Engine Weight, net dry (approx)	757.5 kg (1670 lb)
Power Density	10.7 kg/kW (17.6 lb/bhp)
Power per Displacement	13.6 bhp/L
Jacket Water Capacity	16.0 L (4.2 gal)
Lube Oil System (refill)	31.2 L (8.3 gal)
Oil Change Interval	750 hours
Rotation (from flywheel end)	Counterclockwise
Flywheel and Flywheel Housing	SAE No. 1
Flywheel Teeth	156

Fig. 3. The Caterpillar G3304 Gas-Petroleum Engine

To complete a torsional vibration study, the power, the nominal rotational speed, the inertial momentum of crankshaft and flywheel of the Caterpillar engine and the data about the inertial momentum of CU90G screw compressor rotors are necessary, this data was taken from the technical documentation of the engine and compressor. The inertia momentum of the coupling will be taken from the coupling specifications.

The equivalent oscillating system of a shaft line driven by an internal combustion engine is obtained by inserting the dynamic equivalents of the crankshaft crank arms and shaft sections between the parts in which high values of polar moments of inertia are concentrated (flywheel, couplings, rotors, etc.).The dynamic equivalent of a crankshaft crank arm is represented as an equivalent flywheel in which the polar moment of inertia of the crankshaft crank arm and related engine parts is concentrated, located between two sections of shaft equivalent in half length and zero mass, represented by K letter in the figure 4 [8-10].

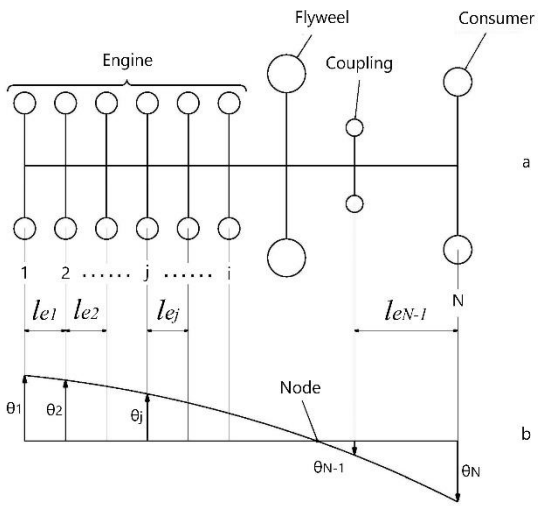

Fig. 4. Oscillating system equivalent of a serially connected shafts with its dynamic equivalent

The equivalent oscillating motor line system of the presented motor-compressor group with an inline 4 - cylinder thermal engine is shown in figure 5, similarly with figure 4.a.

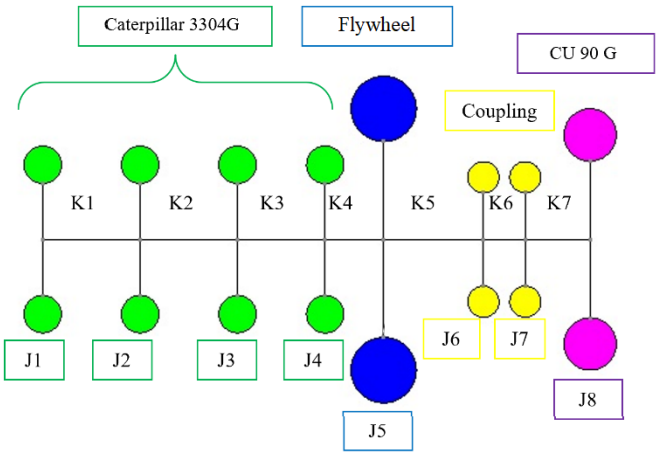

Fig. 5. The oscillating system equivalent to the shaft line of an 8-equivalent flywheels Caterpillar – CU90G compression group

The values J1, J2, J3, J4, J5 are given in [2], J6 and J7 are given in the technical data sheet of the coupling, and J8 was calculated using the masses and diameters of the CU90G screw compressor rotors. The values K1, K2, K3, K4 are taken from [2]. K5 and K7 were determined through calculations using the clutch shaft lengths of the ICE and the screw compressor, respectively. In the case of the clutch shaft, the clutch was neglected in the calculation by considering the shaft longer, see figure 5 above.

In order to find out the value K6, J6 and J7, the size of the coupling corresponding to the P=71kW power of the ICE (Internal Combustion Engine) was determined, as well as the maximum operating speed, according to the relations below:

The torque for the coupling calculation is given by the relation from [11]:

$$M_c = 9550\frac{P}{n}\left[\frac{kW}{rot/min}\right] \quad \textbf{(1)}$$

The work moment necessary to be transmitted, in Nm, is given by the relation:

$$M_w = M_c \cdot C_s \quad \textbf{(2)}$$

where, Cs is a dimensionless safety factor, and according to [11] can be considered for uniform operation with small and rare shocks and light and short overloads, specific to compressors driven by internal combustion engines with 4 or more cylinders, with a value between 1.95 and 2.15. A coefficient Cs = 2 was chosen, and the work moment necessary to be transmitted, in Nm is:

$$M_w = 753.4\ [Nm] \tag{3}$$

From [12], have been chose a 775 Nm value, that corresponds to a size 30 (AX) for the coupling, see figure 6 below.

For a coupling size of 30, we have: J6 = J7 = 0.01938/2 = 0.00992 kgm^2 (Nms^2) and K6 = 3.25x10^5 Nm/rad.

The simplest method of iteratively calculating the pulsations of the shaft line is the one developed by Holzer [13], which is based on the general condition of free vibration in the equivalent oscillating system, namely that the sum of all torques corresponding to the flywheel inertia, the equivalent oscillating system is zero, see the equation 4:

$$\sum_{j=1}^{N} J_j \omega^2 \Theta_j = 0 \tag{4}$$

Having the data for J_j and K_j, the Holzer table can be compiled, starting the iteration with a value ω = 500 rad/s. The amplitude of the first flywheel is considered $\Theta_1 = 1$.

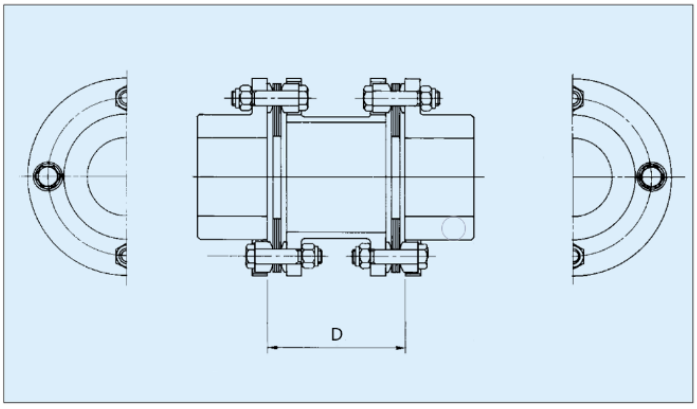

The standard dynamic balance of this coupling is in accordance with JIS G-6.3 (1,800 rpm).

Specifications

Coupling size 30

Common Factors AX, A4, AB				AX				A4			
Size No.	Torque (N•m)	(1) Maximum Rotation (min^{-1})	(2) Axial Spring Constant (N/mm)	D (mm)	Mass (kg)	Moment of Inertia J (kg•m^2)	Torsional Stiffness (N•m/rad)	D (mm)	Mass (kg)	Moment of Inertia J (kg•m^2)	Torsional Stiffness (N•m/rad)
05	33	47,000	21	36	1.1	0.00045	1.1×10^4	88.9	1.2	0.00045	0.9
10	90	39,000	29	39	1.7	0.00103	3.0×10^4	88.9	1.9	0.00110	2.7
15	177	34,000	71	47	2.7	0.00198	7.1×10^4	101.6	2.9	0.00210	6.1
20	245	30,000	83	53	3.7	0.00340	11.4×10^4	127.0	4.1	0.00370	9.3
25	422	25,000	109	62	6.6	0.00943	20.2×10^4	127.0	7.1	0.00990	17.1
30	775	22,000	153	69	10.3	0.01938	32.5×10^4	127.0	10.8	0.02000	27.7
35	1270	19,000	178	78	15.6	0.04070	61.4×10^4	127.0	16.3	0.04200	55.1
40	2060	16,000	220	89	24.0	0.08293	97.7×10^4	139.7	24.7	0.08500	87.2
45	3330	15,000	234	97	31.5	0.13570	141.6×10^4	152.4	32.5	0.14000	128.8
50	4900	13,000	269	109	48.4	0.27163	207.5×10^4	177.8	50.0	0.28000	185.9
55	6370	11,000	280	134	73.9	0.50318	274.9×10^4	177.8	75.0	0.51000	255.5

(1) Maximum rotation speeds are based on rim stress.
(2) Values become linear when torque changes while within the zone of maximum allowable torque specified in this catalog.
(3) Spacers in accordance with ISO standards are available; extra-short spacers under the minimum length spacer are also available.

Fig. 6. Identification of the coupling size

3. CALCULATIONS AND RESULTS

The equivalent oscillating system of a shaft line can execute free torsional vibrations so that, at a given moment, the angular deformations measured next to each equivalent flywheel have the values $\theta_1, \theta_2, ..., \theta_N$. By writing the equations of dynamic equilibrium, for each flywheel, we obtain a system of linear differential equations with constant coefficients:

$$\begin{cases} J_1 \cdot \ddot{\theta}_1 + K_1 \cdot (\theta_1 - \theta_2) = 0 \\ J_2 \cdot \ddot{\theta}_2 + K_2 \cdot (\theta_2 - \theta_3) - K_1 \cdot (\theta_1 - \theta_2) = 0 \\ \dots\dots\dots\dots\dots\dots\dots\dots\dots\dots\dots\dots \\ J_j \cdot \ddot{\theta}_j + K_j \cdot (\theta_j - \theta_{j+1}) - K_{j-1} \cdot (\theta_{j-1} - \theta_j) = 0 \\ \dots\dots\dots\dots\dots\dots\dots\dots\dots\dots\dots\dots \\ J_N \cdot \ddot{\theta}_N \dots\dots\dots\dots\dots\dots - K_{N-1} \cdot (\theta_{N-1} - \theta_N) = 0 \end{cases} \quad \textbf{(5)}$$

For the calculation of the torsional rigidity, the formula from equation (2) was used:

$$K_j = \frac{GI_{pe}}{l_{ej}} = G\frac{\pi}{32}\frac{d_e^4}{l_{ej}} \cdot 10^{-3} \ \ [Nm/rad] \quad \textbf{(6)}$$

When the oscillating system vibrates freely with its own pulsation ω, the equivalent flywheels J_j (j = 1,2, ..., N) performs harmonic vibratory movements with the amplitude Θj and the pulsation ω, so that the angular deformations near these flywheels have, at a given moment, the values:

$$\begin{cases} \theta_1 = \Theta_1 cos\omega t \\ \theta_2 = \Theta_2 \ cos\omega t \\ \dots\dots\dots\dots\dots\dots\dots \\ \theta_N = \Theta_N cos\omega t \end{cases} \quad \textbf{(7)}$$

It is finally obtained through derivation in relation to time a system of N linear equations with unknown N-1: the N vibration amplitudes of the equivalent flywheels Jj (j = 1,2, ..., N) and the own pulsation of the oscillating system ω.

$$\begin{cases} (K_1 - J_1 \cdot \omega^2) \cdot \Theta_1 - K_1 \cdot \Theta_2 = 0 \\ -K_1 + (K_1 + K_2 - J_2 \cdot \omega^2) \cdot \Theta_2 - K_2 \cdot \Theta_3 = 0 \\ \dots\dots\dots\dots\dots\dots\dots\dots\dots\dots\dots \\ -K_{j-1} \cdot \Theta_{j-1} + \left(K_{j-1} + K_j - J_j \cdot \omega^2\right) \cdot \Theta_j - K_j \cdot \Theta_{j+1} = 0 \\ \dots\dots\dots\dots\dots\dots\dots\dots\dots\dots\dots \\ K_{N-1} \cdot \Theta_{N-1} + (K_N - J_N \cdot \omega^2) \cdot \Theta_N = 0 \end{cases} \quad \textbf{(8)}$$

For the system of equations (8) to be compatible, it is necessary that its determinant Δ to be zero, resulting in an equation of N degree in ω^2 [8], which admits an uninteresting root ω = 0 and distinct N-1 roots, of finite value that characterizes the N-1 vibration modes that the N-flywheel oscillation system can perform.

MathCAD software was used to perform these iterations.

The iterative calculation involves finding a value 0 or close to 0, being allowed values up to 0.001×10^6 Nm for the sum of all torques, according to the relation (4). The values calculated for ω = 188.5 rad/s corresponding to 1800 rpm, are given in table 1.

Table 1. Systematization of calculations for the determination by successive tests of the natural pulsation of a line of directly coupled shafts starting from ω = 500 rad / s

Equivalent Flywheel	J_i	$J_i\omega^2$x10^6	Θ_i	$\sum_{i=1}^{k} J_i\omega^2\Theta_i$x10^6	K_ix10^6	$\frac{1}{K_i}\sum_{i=1}^{k} I_i\omega^2\Theta_i$
	Nms^2	Nm	rad	Nm	Nm/rad	-
1	0.0893	0.003173	1	0.003173	1.877	0.002
2	0.0893	0.003173	0.998	0.006335	1.877	0.003
3	0.0893	0.003173	0.995	0.009471	1.877	0.005
4	0.0893	0.003173	0.99	0.01256	3.17	0.004
5	2.435	0.08652	0.986	0.04265	7.85	0.125
6	0.00992	0.000352	0.861	0.001821	3.25	0.302
7	0.00992	0.000352	0.559	0.001379	2.684	0.367
8	0.0433	0.001539	0.192	0.002364	-	-

It is observed that the values of the sum of the torque in column 4 are all positive, which requires the resumption of iterations until a negative value is found. Under the value of 1800 rpm, all the values are positive. Resuming the algorithm, a value of ω of 211 rad/s, corresponding to 2014.9 rpm was reached, see table 2, in which a negative component appeared, very close to ω = 210 rad/s, corresponding to 2005.3 rpm at which all values are positive. The value is about 12% greater than the value of the rotational speed of the assembly.

Table 2. Systematization of calculations for the determination by successive tests of the natural pulsation of a line of directly coupled shafts starting from ω = 211 rad / s.

Equivalent Flywheel	J_i	$J_i\omega^2$x10^6	Θ_i	$\sum_{i=1}^{k} J_i\omega^2\Theta_i$x10^6	K_ix10^6	$\frac{1}{K_i}\sum_{i=1}^{k} I_i\omega^2\Theta_i$
	Nms^2	Nm	rad	Nm	Nm/rad	-
1	0.0893	0.003976	1	0.003976	1.877	0.002
2	0.0893	0.003976	0.998	0.007935	1.877	0.004
3	0.0893	0.003976	0.994	0.01185	1.877	0.006
4	0.0893	0.003976	0.987	0.0157	3.17	0.005
5	2.435	0.1084	0.982	0.5325	7.85	0.156
6	0.00992	0.000441	0.827	0.00219	3.25	0.377
7	0.00992	0.000441	0.449	0.001388	2.684	0.458
8	0.0433	0.001928	-0.009	-0.000135	-	-

The table 2 shows the value of Θ=0.449 rad/s near the flywheel 7 and the negative value of Θ=-0.009 rad/s near the flywheel 8 which indicates an inflection point near the coupling, on the compressor shaft.

Continuing iterations, for a value of ω=287 rad/s have been descovered an inflection point between flyweel 6 and 7, corresponding to a rotational speed of 2740.6 rpm. In installations that use elastic couplings, the torsional rigidity of the coupling is much smaller than the torsional rigidities of the shafts, so that the first vibration mode has nodes placed in the coupling. Have been not found vibrational modes for rotational speeds in the working field of the screw compressor - Caterpillar engine system.

The graph showing the relative amplitudes of the torsional vibrations near the flywheels of the equivalent oscillating system, by the ratio of the values Θ_i to the modulus of the maximum value see the equation (9), is shown in figure 7 obtained by calculations, and has a shape similarly with the theoretical graph from the figure 4.b, as specified in the literature.

$$\Theta_i = \frac{\Theta_i}{|\Theta_8|} \text{ [-]} \tag{9}$$

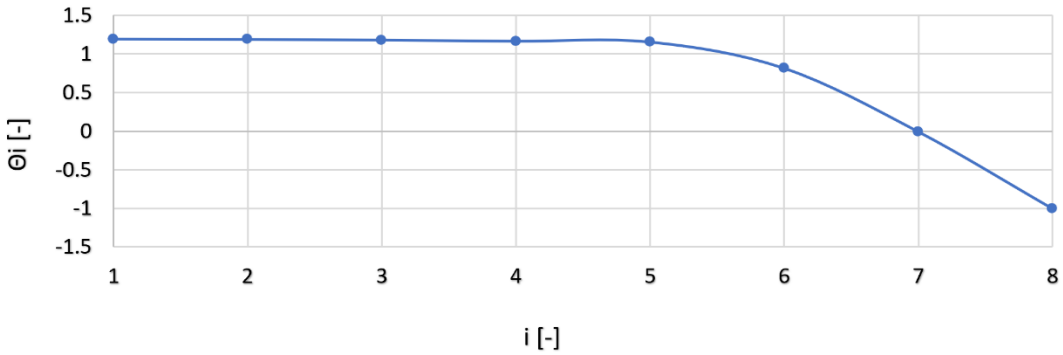

Fig. 7. Relative amplitudes of torsional vibrations

4. CONCLUSIONS

In the paper, a torsion study was performed for the entire system consisting of drive motor and compressor. In order to determine the free torsional vibrations that appear in the shaft line of the two machines coupled using an elastic coupling, an equivalent oscillating system of the shaft line with the Holzer method was taken into account.

Torsional vibrations occur during starting, stopping but also when operating in stationary mode at nominal mode. Thus, the torsional characteristics of the piston equipment must be analysed and evaluated to ensure the safety of its operation. The pronounced torsional vibrations often lead to noises or premature wear of the coupling and if certain limits that are exceeded can lead to breaking the gear teeth, of the shaft keys and even the breaking of the shaft. The response of the components to the torsional vibrations is an important consideration in defining the reliability of the equipment. In order to make a proper analysis, all the forces, moments, but also the elastic and mass properties of all components such as shafts, coupling, gears, rotors, etc. must be taken into account. API standards (610, 611, 617) specify that the torsional vibration modes for the entire equipment may be at least 10% less than any working speed. In some cases, multiples of certain frequencies may occur such as working speed, compression pulses may induce free vibrations. The calculated natural frequency ω = 287 rad/s = 2740.6 rpm is 1.52 larger than the frequency corresponding to the nominal working speed of 1800 rpm for the motor compressor assembly, namely the nominal working speed of 1800 rpm driving the screw compressor. The result shown that the difference between the calculated natural frequency and the frequency corresponding to the nominal rotational speed is greater than 10% of the frequency corresponding to nominal operation complying to the API recommendation. Have been not found vibrational modes for rotational speeds in the working field of the screw compressor - Caterpillar engine system, up to 1800 rpm, the nominal working speed. In the assembly design will be necessary to be taken into consideration the determined value, in choosing the rotation speed of the male rotor of the CU 64 G compressor unit, in conformity with the figure 2, above, in order that its speed do not interfere with the calculated vibrational mode. Future research is focused on bigger capacity compressors and more powerful petroleum-gas engines, in the range of 400 ÷ 700 kW, to achieve the interest of the large petroleum-gas industry companies for autonomous operation and mobile applications.

ACKNOWLEDGEMENT

This research has been developed within the framework of “NUCLEU” Program 2N/2019, “Cercetări avansate asupra sistemelor de propulsie și mașinilor paletate rotative, TURBOPROP” (Advanced research on propulsion systems and rotary pallet machines, TURBOPROP), supported by the Romanian Minister of Research and Innovation.

REFERENCES

[1] http://www.comoti.ro/en/Proiect_MASCS.htm?pag=3;

[2] Tehnical Information G3300, G3400, CG137 Gas Engines, Application and Installation Guide, Caterpillar, 2015 -taken from Gas Engine Rating Pro vers. 6.04.00 software;

[3] http://www.comoti.ro/en/Compresoare-cu-surub.htm;
[4] https://www.kompresory-servis.sk/files/ghh-rand/ghh-product-brochure-en.pdf;
[5] http://www.comoti.ro/img/ATEX_Certificare_compresoare.pdf;
[6]https://www.finning.com/en_CA/products/new/power-systems/industrial/gas-engines/18449959.html
[7] Installation and Initial Start Up Procedures for G3300 and G3400 Engines, Catterpillar - Special Instructions - REHS 0371, 1999
[8] Francis A. B.; 2014; Experimental, Numerical and Analytical Characterization of Torsional Disk Coupling Systems; A Tesis; University of Wisconsin-Milwaukee;
[9] Feese T.P.E. and Hill C. L.; 2002; Guidelines for preventing torsional vibration problems in reciprocating machinery, Gas Machinery Conference, Nashville, Tennessee;
[10] Taraza D.; 1985; Editura didactică și pedagogică; *Dinamica motoarelor cu ardere internă (Dynamics of internal combustion engines)*;
[11] DIN740-2, Power transmission engineering; flexible shaft couplings; parameters and design principles;
[12] http://www.daidoseimitu.co.jp/kata/rist/pdf/form_flex/coupling2.pdf;
[13] Holzer, H.; 1921; Julius Springer Verlag; Die Berechnung der Drehschwingungen; doi:10.1007/978-3-642-51387-9

DEVELOPMENT OF A TRANSPORT AND STORAGE CONTAINER FOR A SPACE OPTICAL INSTRUMENT

Ionuț-Florian POPA[1], Dragoș MIHAI[1], Gheorghe MEGHERELU[1], Radu MIHALACHE[1], Emil NUȚU[2]

Received: 28.10.2021
Accepted: 20.11.2021
Published: 20.12.2021

Copyright: The article is an Open Access article and it is distributed under the terms and conditions Creative Commons Attribution (CC BY) license (**https://creativecommons.org/licenses/by/4.0/**).

ABSTRACT: PROBA-3 is a space mission coordinated by ESA and devoted to the in-orbit demonstration of a precise formation flying techniques and technologies for future ESA missions. Under this mission, one of the primary payloads is the ASPIICS, an optical instrument which makes use of the formation flying technique to form a giant coronagraph capable of producing an eclipse which allows observing the sun corona closer than ever before. Considering the fact that the ASPIICS instrument is an optical type one, it is also very sensitive to handle, requiring a dedicated mean for manipulation and transport. COMOTI was selected by the Centre Spatial de Liege to develop a dedicated container which shall facilitate the manipulation and transport of the ASPIICS instrument for assembly, integration and testing activities between different sites in Europe, until the final integration on the Coronagraph satellite. Starting from a dedicated set of requirements, COMOTI designed, manufactured, assembled and tested a custom product consisting of two enclosures which shall protect the ASPIICS instrument against contamination (dust particles, humidity) and mechanical loads. The developed Mechanical Ground Support Equipment (MGSE) demonstrated the ability to ensure its tightness following a pressure test, thus validating one of its main functions, and it was delivered to the beneficiary to be used for its intended purpose.

KEYWORDS: optical instrument, transport and storage container, Mechanical Ground Support Equipment

1. INTRODUCTION

The development of a space product requires, at a certain point, a series of equipment which are used either for assembly, integration or testing, in order to ensure that the product complies with the mission's requirements. These are called Mechanical Ground Support Equipment (hereinafter referred to as MGSE), being used for assembly, integration and testing activities (vertical or horizontal trolleys, tilting trolleys, adapters), manipulation (lifting devices), physical properties evaluation (CoG – Centre of Gravity adapters, calibration devices) or transport (containers). Several examples of MGSE items for the space industry are presented in Fig. 1.

[1] Romanian Research and Development Institute for Gas Turbines COMOTI
[2] "Politehnica" University of Bucharest, Department of Strength of Materials

Vertical integration trolley *Satellite tilting trolley* *Satellite transport container* *Satellite lifting device*

Fig. 1. MGSE items for space industry (images credit: ESA)

PROBA (Project for OnBoard Autonomy) are a series of satellites which aim to validate new techniques and technologies for future ESA missions [1]. The first PROBA mission was launched in October 2001 [2], as a technology demonstration mission, and it still operating as an Earth Observation Third Party Mission. In the following years, two more PROBA missions were launched, Proba-2 and Proba-V, both still operable [3, 4].

PROBA-3 is a mission scheduled to be launched in 2023, consisting of two small satellites (150 ÷ 300 kg) [5], a Coronagraph spacecraft, and an Occulter spacecraft. The pair of satellites will perform the first precision formation flying mission ever, adopting a fixed configuration in space, 144 m apart one from the other. The purpose of this formation flying is to study the Sun's corona, with the help of a scientific instrument, called ASPIICS (Association of Spacecraft for Polarimetric and Imaging Investigation of the Corona of the Sun), which is an externally occulted coronagraph. While the two spacecraft are in orbit, the Occulter is positioned relatively to the Coronagraph in order to produce a nearly perfect eclipse which allows observing the Sun's corona closer to the rim than ever before [6]. Fig. 2 presents the two spacecraft in formation flying and the orbit which they will follow in the mission.

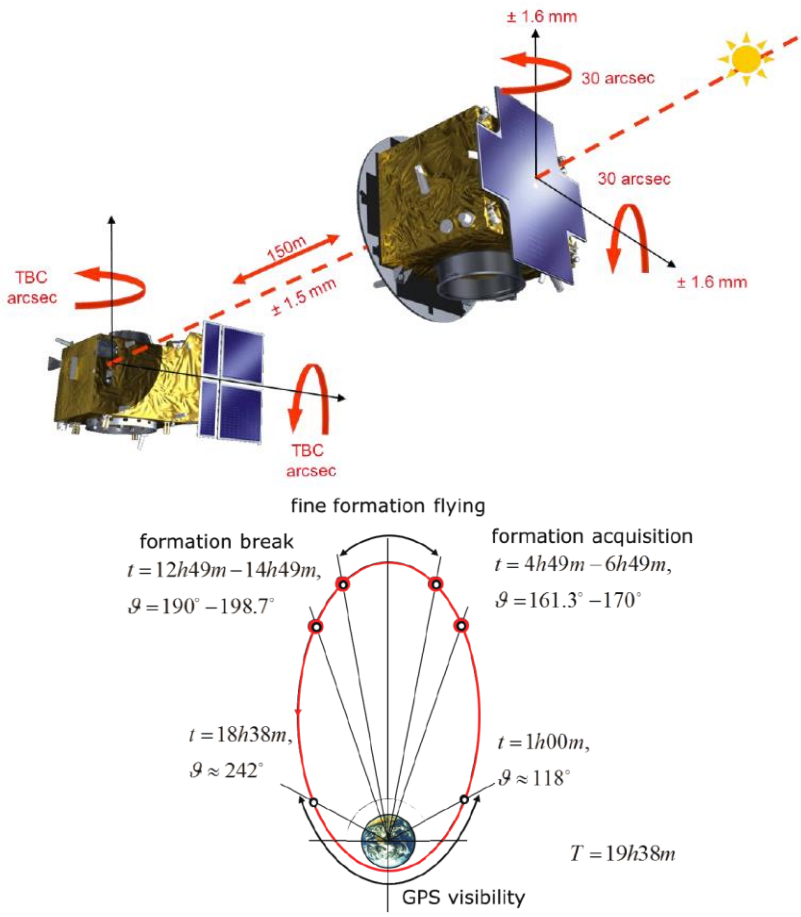

Fig. 2. PROBA-3 formation flying overview and orbit [7]

The Coronagraph instrument consists of several lenses, filters and polarizers which guide the light waves to an optical detector, all mounted in a tubular structure which is presented in Fig. 3. As the ASPIICS instrument is an optical one, requiring high precision in operation, it is also very sensitive to external factors such as dust, humidity, shocks, transport loads etc. Thus, it requires a dedicated container which shall protect it during the assembly, integration and testing activities, as well as for transport and long storage periods.

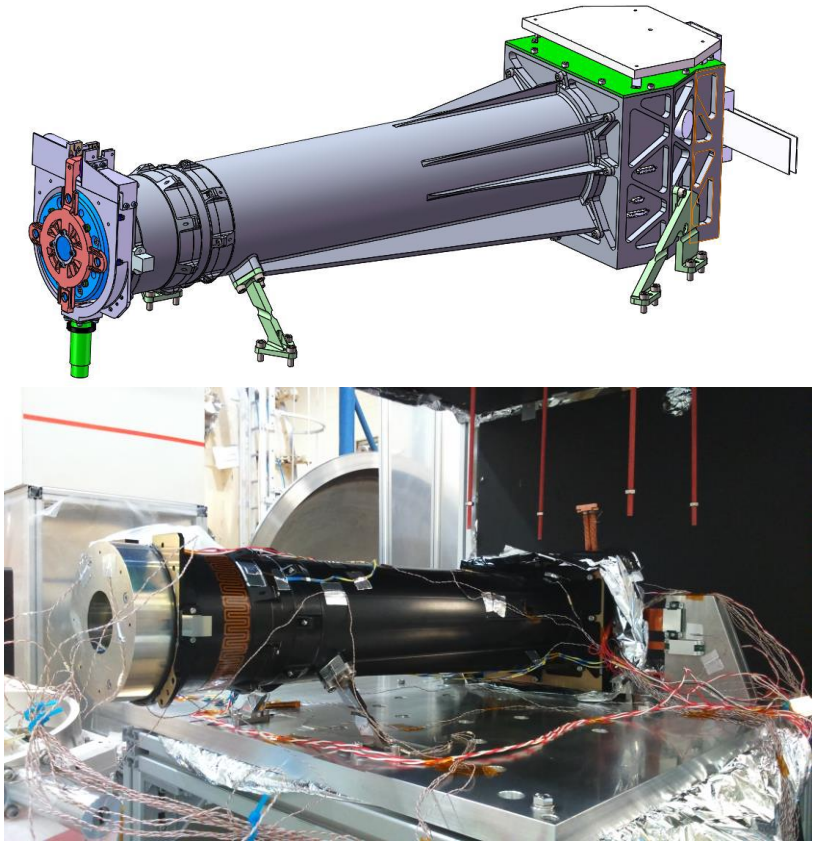

Fig. 3. Coronagraph design: CAD model (top) [8] and Structural Thermal Model (bottom) [9]

Containers for transportation and storage of space instruments can have various configurations, shapes and sizes, depending on the requirements imposed and the needed level of protection. Thus, these can consist of a single or a double enclosure, as depicted in Fig. 4. Moreover, each container is developed as a custom item, specifically designed for its particular application.

Single enclosure container [10]

Double enclosure container [11]

Fig. 4. Types of transport and storage containers for space instrument

2. ASPIICS CONTAINER REQUIREMENTS

Being a custom product, the ASPIICS container development starts from a comprehensive set of requirements imposed by the Centre Spatial of Liege, which is in charge with the development of the ASPIICS instrument. The most important requirements are resumed in Table 1.

Table 1. Driving requirements for the ASPIICS instrument container

No.	Requirement description
1	The container shall protect the Coronagraph System during storage and transport in terms of: - Contamination (Molecular and Particulate); - Outside environment (handling loads, humidity, ...). The inside contamination environment shall be better than ISO 5 cleanrooms.
2	The container shall be composed of two distinct envelopes: - Outer envelope, for protection from shocks and external environment; - Inner envelope, for protection from particulate and molecular contamination, as well as humidity.
3	The inner envelope shall be mechanically decoupled from the outer envelope by a spring system to reduce any shock due to handling.
4	The inner envelope is directly around the Coronagraph System. It shall be hermetically sealed and purgeable with dry nitrogen. The nitrogen environment will be at a small overpressure of 50 mbar with respect to the atmosphere. To this purpose, FESTO connectors shall be implemented for nitrogen purging and a manometer shall be included to monitor the inner pressure.
5	The inner envelope allocated for the Coronagraph System inside the container shall be at least the following: - 1300 x 570 x 390 mm (Length x Width x Height).
6	A mechanical interface shall hold the Coronagraph System in place. The interface shall be as defined in the Mechanical Interface Control Document.
7	No part of the container shall touch the Coronagraph System at any time with the exception of the dedicated interface.
8	2 guiding bars shall be implemented to prevent collision between the lid and the Coronagraph System during (un-)packing.
9	The tolerances on the mechanical interfaces defined in requirement no. 6 are: - Roughness 0.8 µm; - Flatness 0.1 CZ.
10	The overpressure in the inner envelope will be done in a cleanroom at a pressure between 970 mbar and 1050 mbar. The sizing of the container shall consider that the inner envelop could be at a pressure of 1100 mbar while the outer container would be at 970 mbar as well as the inner envelop pressure could be at 1020 while the outer container would be at 1050 mbar. A safety valve should be implemented on the inner envelope to avoid reaching a differential pressure out of design range.
11	The outer envelope shall be cleanable with alcohol and vacuum cleaner to allow entering ISO 7 (class 10 000) cleanrooms. The inner envelope will be cleanable with alcohol, acetone and vacuum cleaner to allow entering ISO 5 (class 100) cleanrooms.
12	The environment during transport handling is defined as: - Vertical loads: +- 3.0g; - Horizontal loads: +- 2.0 g; - Shock: +- 4.0g, 20ms, Saw Tooth; - Temperature: -40°C to +60°C; - The transport duration can be up to 1 week.

Considering the requirements defined above, a container for the transport and storage of the ASPIICS instrument was designed and manufactured by COMOTI. Its design and main particularities are presented in the following sections.

3. CONTAINER DESIGN AND STRUCTURAL ANALYSIS

The first requirement which drives the configuration of the container design is requirement 2, which states that the ASPIICS container shall consist of a two-enclosure system, having different roles (first one

protects against dust and particulate contamination, second one against rain, humidity and handling loads. The two enclosures are presented in the following section.

3.1. Inner envelope – metallic container

The inner envelope consists of two main parts: a bottom plate assembly made of aluminium alloy type 7075, on which the instrument with its transport plate are mounted, and a lid assembly made of stainless steel, cylindrical in shape and foreseen with torospherical caps at the ends. The overall design of the inner envelope is presented in Fig. 5 and Fig. 6. Note that the initial dimensions specified in requirement 5 were initially leading to a very large container compared to the dimensions of the instrument. In order to reduce the mass and optimize the dimensions of the container, it was agreed to reduce these values up to the point where there are at least 100 mm between the ASPIICS instrument and the inner container inside in any point given.

Considering that this envelope houses directly the sensitive optical instrument, including the one which will fly, a particular attention was paid to the choosing of materials so that they are compatible with the ISO5 cleanroom conditions, as well as easy cleanable.

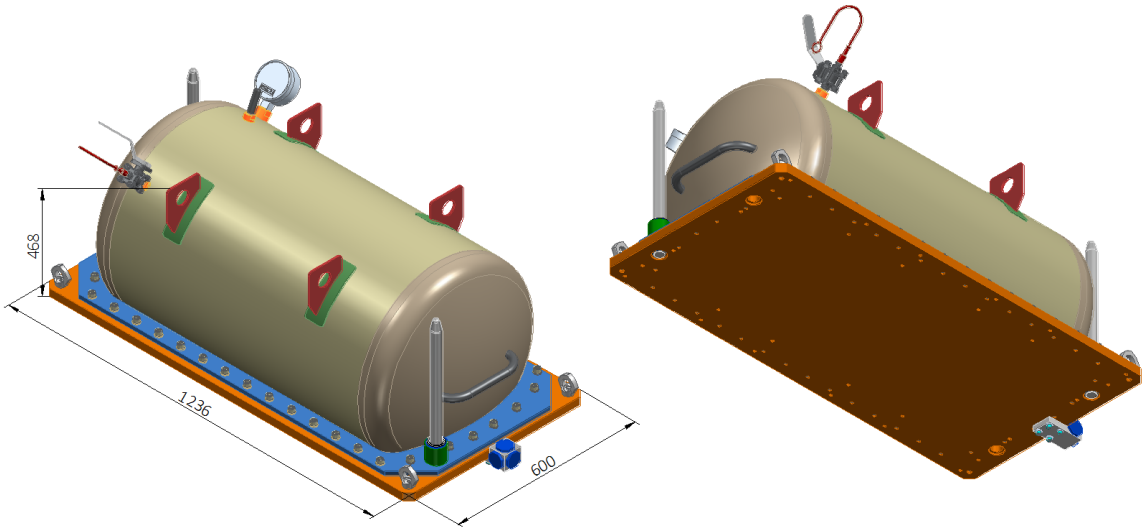

Fig. 5. Inner envelope in closed configuration

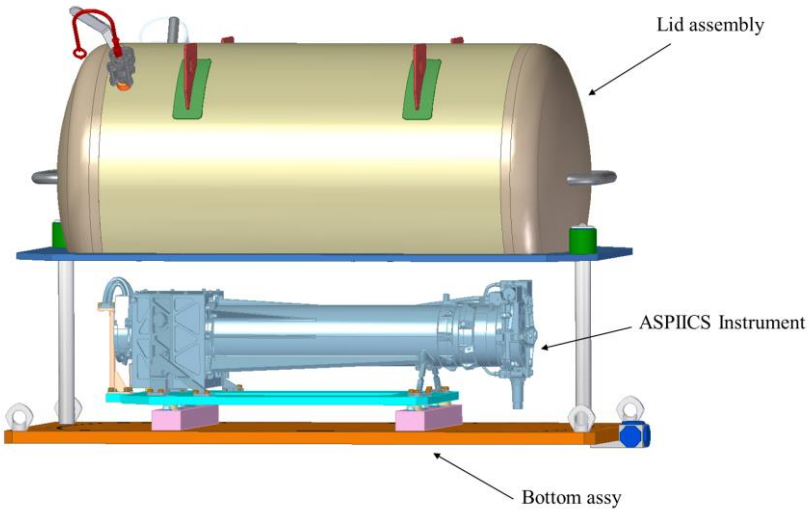

Fig. 6. Inner envelope in open configuration – side view

The inner bottom assembly consists of an aluminium alloy plate (orange) holding the platform (light blue) on which the ASPIICS instrument is mounted (Fig. 7). Two guiding bars are foreseen to guide the lid assembly during the closing and opening of the container, in order to avoid hitting the instrument. The manipulation of the inner envelope can be made by means of four rotating hoisting rings, placed in each corner

of the plate. The sealing of the inner envelope is ensured by a Ø7-mm O-ring placed in a groove machined on the inner bottom assembly plate. The sealing design (Fig. 8) is based on recommendations and guidelines stated in reference [12].

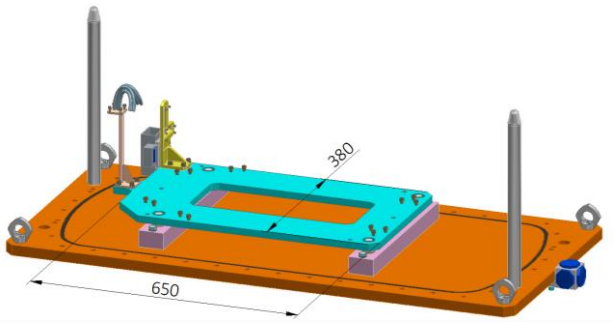

Fig. 7. Inner envelope bottom assembly – isometric view

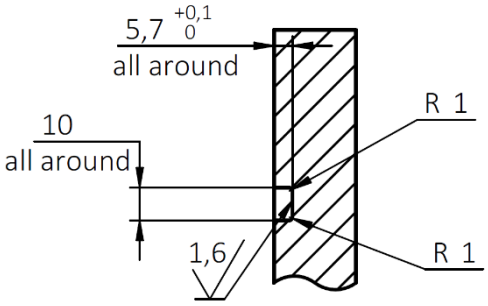

Fig. 8. Inner envelope sealing groove design and dimensions

The lid assembly is made entirely of 316L stainless steel welded parts, consisting of the flange, a cylindrical wall, 2 torospherical end caps Ø550 mm (acc. to DIN 28011), 4 lifting supports and 2 handles, as depicted in Fig. 9. The lid flange is foreseen with two holes on which two pipe segments (marked with green) are welded. These correspond to the guiding bars foreseen on the bottom assembly.

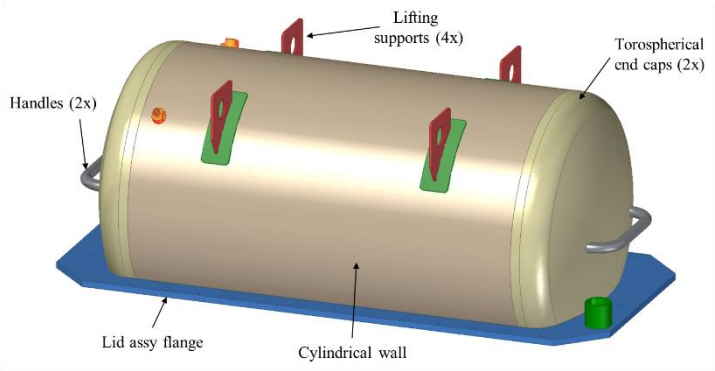

Fig. 9. Lid welded assembly

3.2. ASPIICS Instrument Platform

When storing the ASPIICS instrument, the inner envelope base plate suffers deformations due to the pressure inside which can be higher or lower than the external one. In this regard, a rigid mounted platform is foreseen on the base plate, mounted on two aluminium blocks, as it can be seen in Fig. 10. The instrument platform features also two interfaces necessary to mount the electrical and thermal interfaces of the ASPIICS instrument. These are shown in Fig. 11.

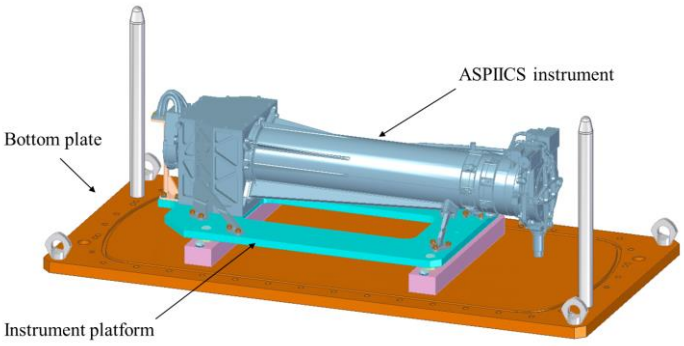

Fig. 10. ASPIICS instrument platform place on the inner envelope base plate

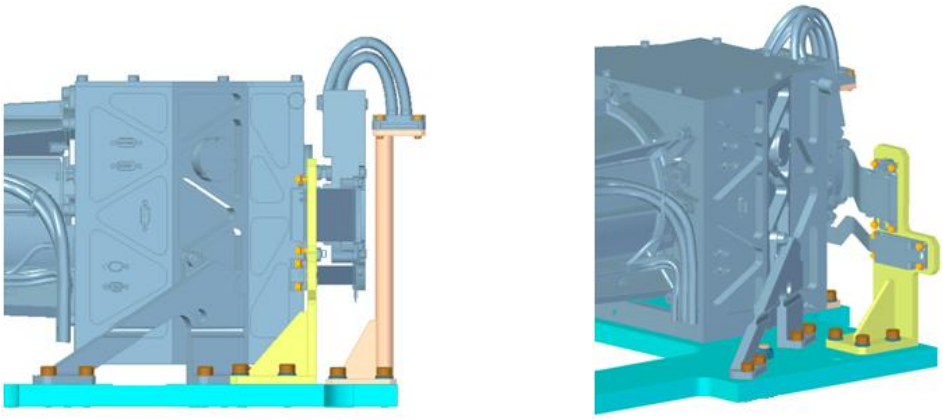

Fig. 11. Details of block strap (peach) and block connectors (yellow) supports

3.3. ASPIICS inner envelope structural analysis

As specified above, during transport (land or air) of the ASPIICS instrument with the container, it is expected that the pressure inside the inner envelope will determine the base plate to deform. This effect can cause deformation to the instrument platform through its support, leading to potential instrument damage. In order to check if the planarity of the instrument plate is ensured under an internal pressure of 350 mbar (0.035 MPa), a finite element analysis of the inner envelope was performed.

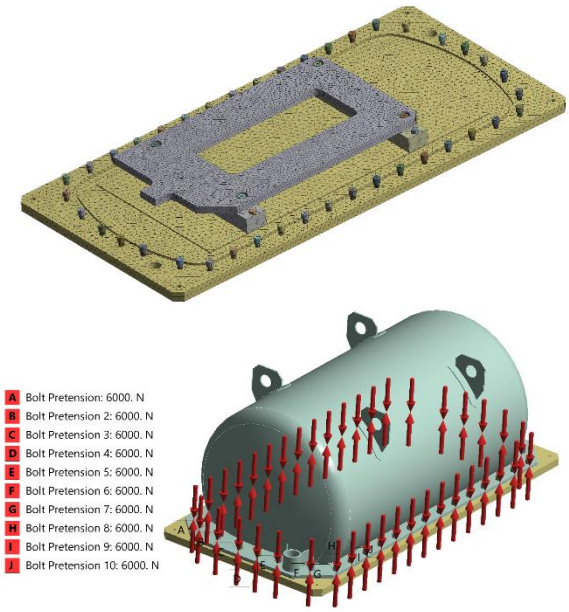

Fig. 12. Inner envelope bottom assembly – mesh model and boundary conditions

The mesh model used for the FEM calculus is presented in Fig. 12. The model features a total of 677922 elements (higher order tetrahedrons) and 1104334 nodes. As boundary conditions, an internal overpressure of 350 mbar was considered in the model. Also, each bolt was pretensioned by 6000 N, simulating the assembly between the two main components of the inner envelope assembly.

The overall displacements distribution for the assembly consisting of the base plate and the instrument platform are plotted in Fig. 13. One can notice that the base plate deforms, reaching in the middle to a maximum displacement of 0.045 mm. These deformations cause the instrument platform to displace vertically, without significant deformation, mainly due to the clamping system between the two plates.

Fig. 14 presents the vertical displacements of the instrument platform. The difference between the maximum and the minimum value is 0.0095 mm. This difference indicates the loss of planarity, however below the imposed limit of 0.1 mm. In Fig. 15 the vertical displacements of the contact surfaces between the instrument supports and the platform. The loss of planarity, calculated as the difference between the maximum and minimum displacement values is 0.0082, clearly below the 0.1 mm threshold.

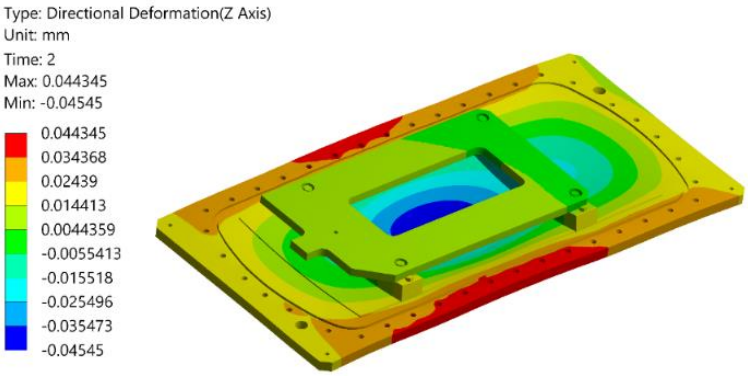

Fig. 13. Inner envelope bottom assembly – overall displacements

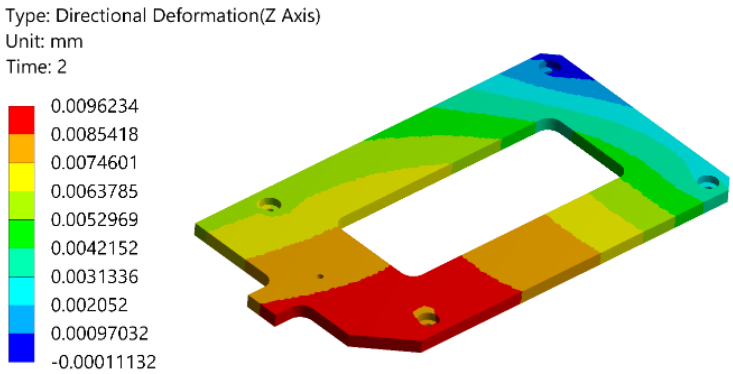

Fig. 14. Instrument platform – vertical displacements

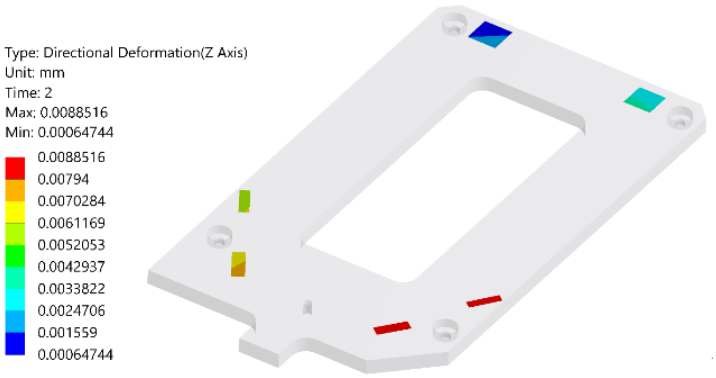

Fig. 15. Vertical displacements of the contact surfaces between the instrument supports and the instrument platform

3.4. ASPIICS Outer envelope

The outer envelope protects the inner one against shocks and external environment (weather, handling loads). Having in mind the configuration of the inner envelope, the outer one was designed as a container with a low base and a tall lid, as presented in Fig. 16. This configuration allows an easy integration of the inner envelope.

The outer envelope consists of two main parts: the chassis and the outer envelope box. For weight purposes, the outer envelope box is a flight case (approved for road or aerial transportation) with walls made of polypropylene panels (material called Astroboard [13]) assembled with L aluminium profiles. As the outer envelope box cannot sustain the entire weight of the inner envelope (approx. 147 kg), a special welded chassis was designed, made of IPE100 stainless steel profiles (Fig. 17). On this chassis the low base of the outer envelope box was integrated as shown in Fig. 18.

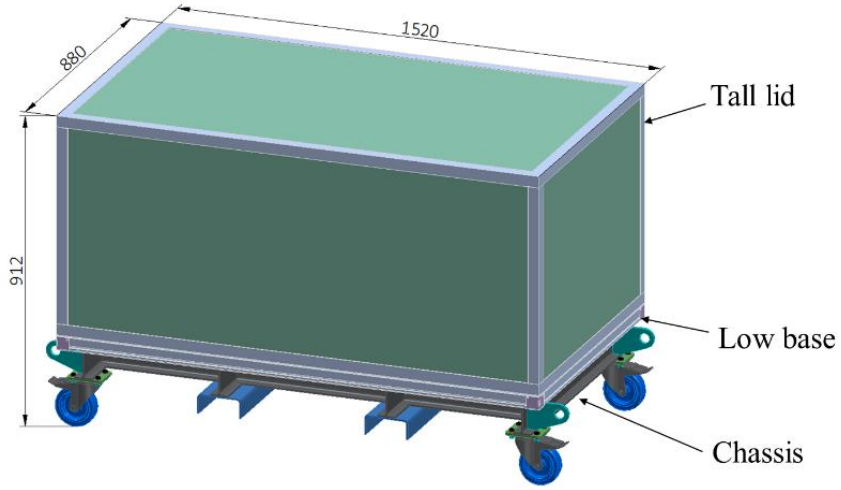

Fig. 16. Outer envelope isometric view

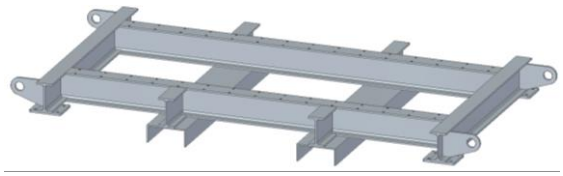

Fig. 17. Outer envelope welded chassis

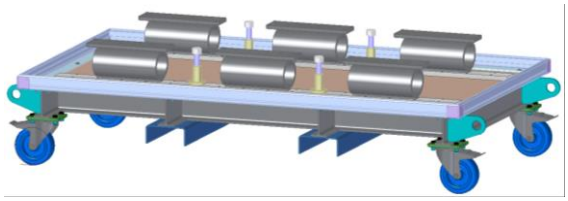

Fig. 18. Outer envelope chassis assembly containing the welded chassis and the low base

As stated before, the outer box is made of polypropylene sandwich panels (supplied from CON-PEARL Germany), which are 40% lighter than their equivalent in wood panels, and aluminium L profiles for the edges. A section through the material is presented in Fig. 19.

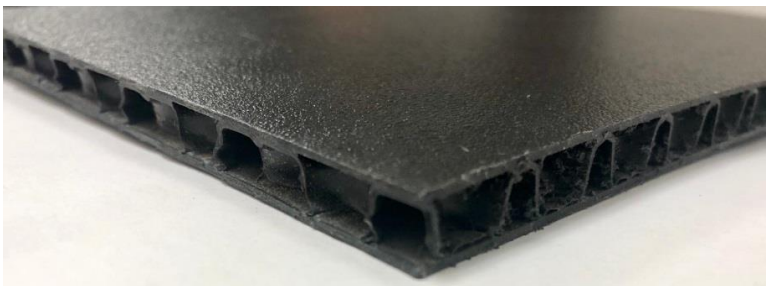

Fig. 19. Polypropylene sandwich panels

4. CONTAINER ACCESSORIES AND SPECIAL DEVICES

During the transport activities, the optical instrument can be affected by the mechanical environment encountered. One method to prevent this issue is to include vibration dampers in the container's structure.

Starting from the requirement regarding the transport conditions, an analysis was employed to determine the best configuration and size for the vibration dampers. Usually, the state-of-the-art technologies in damping of structures that hold sensitive items such as the ASPIICS instrument presumes using wire rope isolators. Their advantages [14] lie in their ability to combine a high level of isolation in a relatively small space. Also, they can be loaded in any direction without the risk of malfunctioning.

To account for the mechanical loads occurring during transport, a number of 6 wire ropes isolators were foreseen on the bottom of the inner envelope, as depicted in Fig. 20. In Fig. 21 the configuration of the wire rope isolator used and its dimensions are presented.

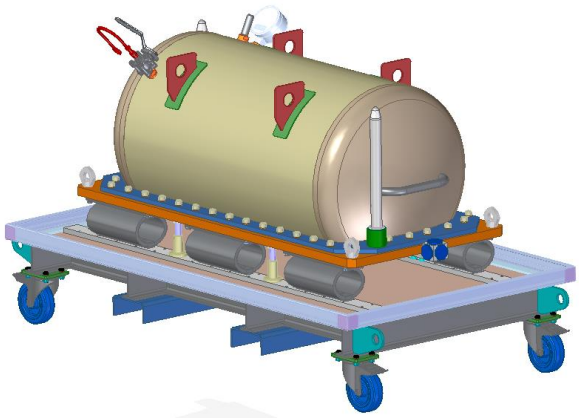

Fig. 20. Inner envelope placed on wire rope isolators

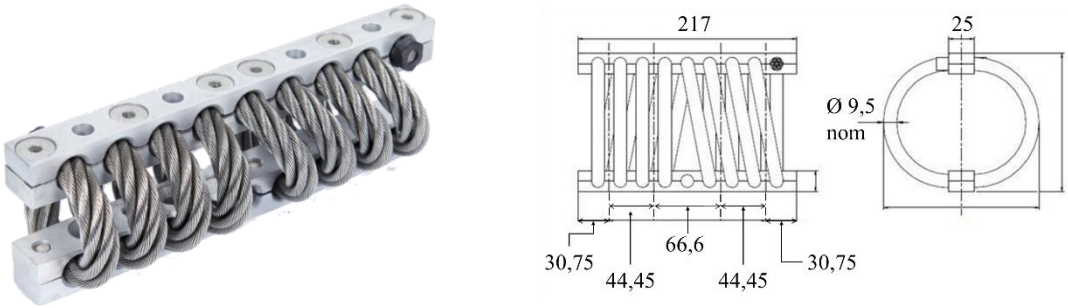

Fig. 21. Wire rope isolator configuration and dimensions

The used wire rope isolators were analysed under harmonic and random loads derived from requirement 12, Table 1, to emulate the transportation conditions. In Fig. 22, there are presented the loads spectra and the frequency response curves (blue and red curves, respectively) obtained by numerical analysis performed by the wire rope isolators supplier (SOCITEC France). The three axes (x, y and z) are associated with the following directions: x indicates the container longitudinal axis, y the transversal horizontal axis, while z represents the vertical axis. For a mass of 160 kg of the inner envelope, including the ASPIICS instrument, the static deflection is 2,9 mm. The value is relatively small with respect to isolator dimensions (Fig. 21), indicating enough stiffness to avoid large amplitudes in the case of vibration excitations.

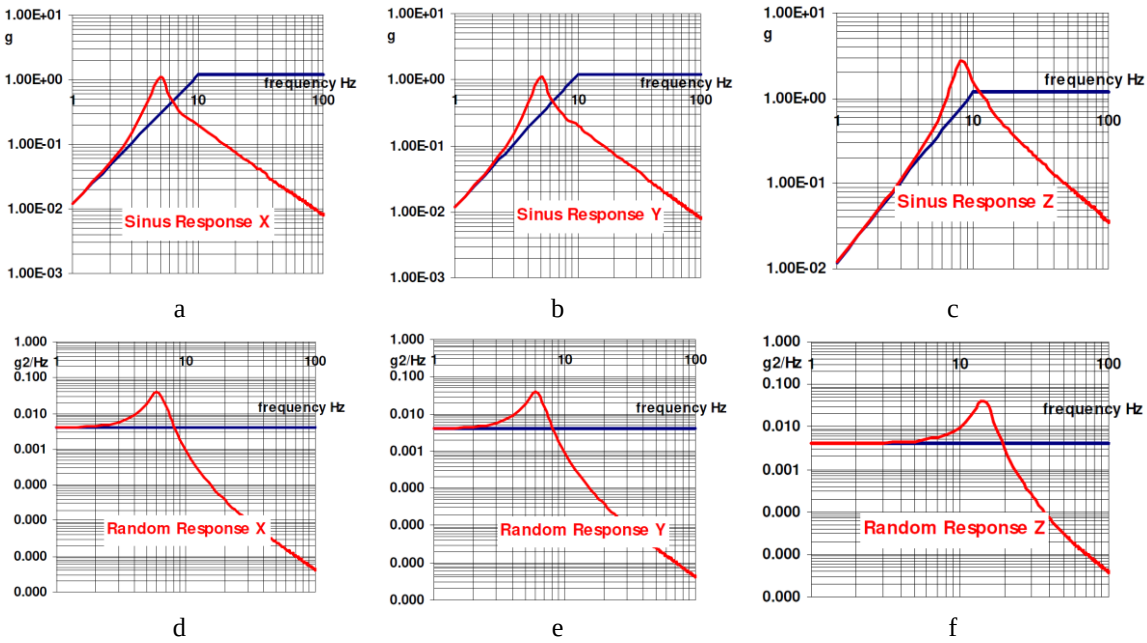

Fig. 22. Sine and random loads results

From Fig. 22, one can notice that each vibrational load case excites only one resonance for the insulators, which occurs at low frequencies: 5 Hz for x and y horizontal harmonic loads (Fig. 22, a and b), 8 Hz for z vertical harmonic loads (Fig. 22, c), 6 Hz for x and y horizontal random loads (Fig. 22, d and e), 10.5 Hz for z vertical random loads (Fig. 22, f). However, the amplitude of vibration is small, bellow the quasistatic imposed requirements (Table 1, requirement 12 – 2g for horizontal loads and 3g for vertical ones). For higher frequencies, the isolators significantly drop the amplitude with respect to the excitation level, indicating good vibrational damping.

The interface between the inner envelope and the six wire rope isolators mounted on the outer base is made by means of 6 stainless steel plates (one for each isolator). The purpose of the plates is to allow an easy mounting/dismounting of the inner envelope assembly, considering that the available space for this operation is small. Each intermediate plate is fixed on the inner envelope assembly by means of four M8 screws.

The inner envelope assembly has a large mass, thus its integration on the outer envelope base can prove difficult, requiring the alignment of the through holes of the intermediate plate with the corresponding threaded holes in the inner envelope base plate. For this purpose, four pillars were implemented on the outer envelope base. The pillars consist in an aluminium part with internal thread, a threaded rod and a PTFE nut locked by a pin.

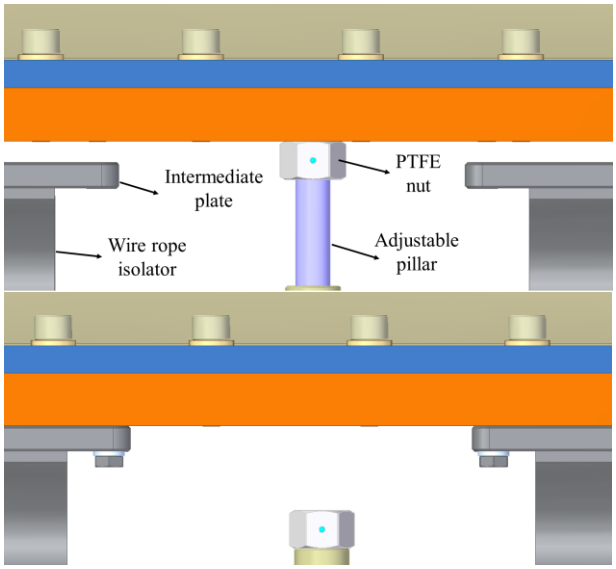

Fig. 23. Inner envelope placing on pillars before and after mounting

As one can see in Fig. 23 left, the inner envelope is placed firstly on the four pillars, being in contact with the PTFE nuts. This material is strong enough to support the entire weight of the inner envelope, while avoiding scratching the bottom surface of the inner envelope base plate. The four pillars are retracted by screwing in the aluminium part, lowering the inner envelope in order to be in contact with the 6 intermediate plates. Before all the weight is taken by the wire rope isolators, the intermediate plates are aligned with the corresponding holes from the inner envelope base, and then screwed on it with M8 bolts as depicted in Fig. 23 right. After the inner envelope is secured on the outer envelope base, the pillars can be completely retracted. The procedure for dismounting is similar.

5. CONTAINER ACCEPTANCE TESTS

According to the requirements, the pressure inside the inner envelope can vary between 970 and 1050 mbar during transport. Also, the space inside will be pressurized with up to 50 mbar of nitrogen gas for cleanliness purposes. Considering the transport scenarios, including by flight, it was decided to perform a static pressure test. The test consists in pressurizing the inner envelope with 250 mbar of compressed air with respect to the atmospheric pressure for 6 days. For each testing day the pressure, temperature and relative humidity of the storage room and the pressure inside the inner envelope were recorded.

The test set-up is presented in Fig. 24. The inner envelope was assembled and screwed in order to form a tight enclosure. The inside pressure is read on the manometer foreseen on the lid. Before starting the actual test, all the ports were checked for eventual leaks.

Fig. 24. ASPIICS inner envelope test set-up

The variation of the relative pressure value, read from the manometer shown in Fig. 24, over the 6 days of the test is plotted on the graph presented in Fig. 25, along with the variation of the atmospheric pressure which was taken from the Romanian Meteorological Administration official data. During the test, the storage room temperature and humidity were also recorded. One can see that the pressure does not vary more than 10 mbar during the entire test campaign. Thus, it is considered that the design implemented for the container is validated in terms of tightness.

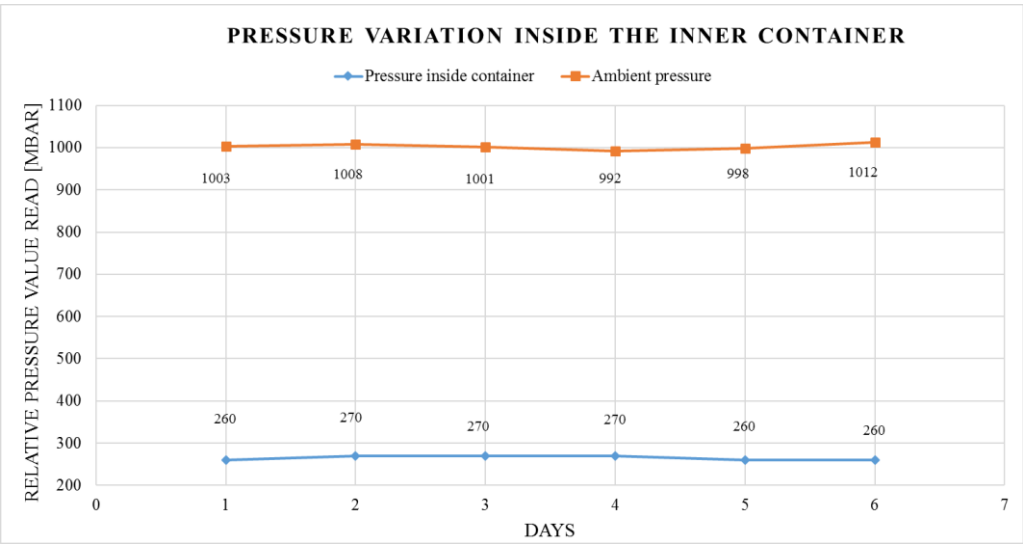

Fig. 25. Relative pressure variation inside the inner envelope

Additionally, in Table 2 are presented the data recorded for the temperature and humidity inside the storage room. There were no significant variations in terms of the ambient conditions during the test.

Table 2. Temperature and humidity measured during the acceptance test

Day no.	Measured temperature	Relative humidity
1	20,3	37
2	20,7	40
3	20,3	41
4	20,1	41
5	20,8	38
6	21,6	36

6. CONCLUSIONS

The transport container developed for the manipulation of the PROBA-3 ASPICS Optical Instrument has proved its compliance with the requirements being successfully used by CSL. The imposed requirements were fulfilled either by design, manufacturing or through the acceptance test performed before delivery.

Furthermore, this confirms that the adopted solutions for the fixing the instrument inside the inner envelope (dedicated platform) and for the vibration damping (wire rope isolators) were proper dimensioned and verified by means of FEM analysis, limiting the mechanical loads transmitted to the instrument. The same thing can be noted for the sealing solutions implemented on the inner envelope, that managed to assure the necessary overpressure (compressed air) for the imposed duration.

As this is a container designed to transport a space equipment from a cleanroom to another, the cleanliness conditions (at least ISO5) had also to be ensured on its surfaces. A special attention was given to the selected materials, manufacturing processes and design oriented to cleanliness (easy access for surfaces cleaning).

The developed product was delivered to Centre Spatial de Liege in March 2020 and it was validated as fully functional for its purpose.

Inner envelope placed on the outer base Outer envelope closed

Fig. 26. ASPIICS Container

ACKNOWLEDGEMENT

The work described in the current paper was financed through a project coordinated by the Centre Spatial de Liege, contract no. P3-CSL-CO-15020.

REFERENCES

[1]. Bermyn, J., PROBA spacecraft family – small mission solutions for emerging applications, *The International Archives of the Photogrammetry, Remote Sensing and Spatial Information Sciences*, Vol. XXXVII, Part B1, Beijing, 2008;

[2]. European Space Agency, *Proba-1 overview*, access link, accessed 08.09.2021

[3]. OSCAR, *Satellite: PROBA-2*, access link, accessed 08.09.2021;

[4]. OSCAR, *Satellite: PROBA-V*, access link, accessed 08.09.2021;

[5]. Llorente, J.S., Agenjo, A., Carrascosa, C., de Negueruela, C., Mestreau-Garreau, A., Cropp., A., Santovincenzo, A., PROBA-3: Precise formation flying demonstration mission, *Acta Astronautica* **82** (2013), pp.38-46, Elsevier, DOI: https://doi.org/10.1016/j.actaastro.2012.05.029;

[6]. Renotte, E., Alia, A., Bemporad, A., Bernier., J et al., Design status of ASPIICS, an externally occulted coronagraph for PROBA-3, *Proc. SPIE 9604, Solar Physics and Space Weather Instrumentation VI*, 96040A, 28 September 2015, DOI: https://doi.org/10.1117/12.2186962;

[7]. Galy, C., Thizy, C., Stockman, Y., Galano, D. et al., Straylight analysis on ASPIICS, PROBA-3 coronagraph, *Proc. SPIE 11180, International Conference on Space Optics — ICSO 2018*, 111802H, 12 July 2019, DOI: https://doi.org/10.1117/12.2536008;

[8]. Renotte, E., Buckley, S., Cernica, I., Denis, F., et al., Recent achievements on ASPIICS, an externally occulted coronagraph for PROBA-3, *Proc. SPIE 9904, Space Telescopes and Instrumentation 2016: Optical, Infrared, and Millimeter Wave*, 99043D (29 July 2016); DOI: https://doi.org/10.1117/12.2232695

[9]. Zukhov, A., PROBA-3 / ASPIICS and its potential synergies with Solar Orbiter / Metis, Solar-Terrestrial Centre of Excellence SIDC, Royal Observatory of Belgium, 22 November 2018;

[10]. Elital Italy, *MGSE – Instrument Transport Containers*, access link, accessed 09.09.2021;

[11]. SENER Poland, *SENER in Poland provides security for the scientific instrument of the European Space Agency's satellite*, access link, accessed 09.09.2021;

[12]. International Standard Organization, ISO 3601-2 – *Fluid power systems – O-rings, Part 2: Housing dimensions for general applications*.

[13]. CON-PEARL, Astroboard material data sheet, https://con-pearl.de/en/con-pearl/, accessed 15.09.2021;

[14]. Trelleborg, *Wire Rope Isolators*, access link, accessed 17.09.2021;

COMPARISON OF DIFFERENT ADDITIVE MANUFACTURING METHODS FOR PRE-EVALUATION OF CENTRIFUGAL PUMP COMPONENTS

Ionut Florian POPA[1], Dragos MIHAI[1], Mihai VLADUT[1], Daniel ASOLTANEI[1]

Received: 29.10.2021
Accepted: 25.11.2021
Published: 20.12.2021

Copyright: The article is an Open Access article and it is distributed under the terms and conditions Creative Commons Attribution (CC BY) license (**https://creativecommons.org/licenses/by/4.0/**).

ABSTRACT: Using the additive manufacturing technology, the development of complex assemblies or individual components can be accelerated with minimum amount of resources (manufacturing time and cost) achieving fully functional parts. However, a comparison must be carried out between different additive manufacturing methods and materials to identify which method offer the most suitable dimensional accuracy, surface quality and tolerances. The current paper presents a comparison between three different additive manufacturing methods that use polymeric materials as feedstock, such as stereolithography, selective laser sintering and Polyjet, in order to pre-evaluate two main components of a centrifugal pump: the impeller and the volute. Each manufactured prototype was dimensionally evaluated using 3D measurement machine in order to identify the dimensional deviations. The roughness of printed parts was measured on the external surface area without applying any post-processing method.

KEYWORDS: closed impeller, volute, polyjet, stereolithography, selective laser sintering

NOMENCLATURE

AM	Additive Manufacturing
CAD	Computer-Aided Design
CFD	Computational Fluid Dynamics
MPFL	Mechanically Pumped Fluid Loop
SLA	Stereolithography (3D printing method)
SLM	Selective Laser Melting
SLS	Selective Laser Sintering
STL	Stereolithography (CAD file)

1. INTRODUCTION

The AM market is one of the fastest growing emerging technology coming to market with a potentially disruptive power. However, the global 3D printing plastics market size was valued in 2019 at 520.5 million USD [1] and it is witnessing high demand, as it is highly efficient as compared to various other traditional manufacturing methods [2]. In the aerospace industry, where the focus is directed towards flight hardware or

[1] Romanian Research and Development Institute for Gas Turbines COMOTI, Bucharest, Romania

manned space missions, a limited number of prototypes were manufactured and validated to be mounted on spacecrafts and airplanes, as the verification, qualification and acceptance process is difficult and drastic. Thus, the impact of AM continues to expand as the technology gains acceptance and functionality in a variety of industries like space, automotive and medical [3].

The development of a complex and sensitive assembly, such as a centrifugal pump designed for MPFL systems, implies multiple design iterations for the critical parts especially if specific performances are targeted. The effort of a complete manufacturing process for a closed impeller using SLM technology is presented by Adiaconitei et al. in [4] and [5]. Even if AM technology presents major advantages in terms of time resources and design freedom, it requires special attention on possible inherent defects as highlighted by Vintila et al. in [6]. Using additive manufacturing methods to fabricate rapidly a scale model of a physical part or assembly and to evaluate the proposed design, enables the design and optimisation activities by reducing the time, efforts, and costs incurred in the development process as presented by the authors in [7]. Prototyping phase is required for assessing the dimensions and geometry, fit and functionality can accelerate the process to achieve a product market. The corrections or variations in design, materials, size, shape, assembly, manufacturability and strength can be made following the results of testing and analysing the prototypes. Numerous different additive manufacturing methods are commercially available, each with its unique strengths [8, 9] and weak points. As prototyping processes continue to evolve, a main concern of the product designers is to define a methodology to select the most suitable prototyping method based on the requirements of the specific application.

This paper aims to explore the advantages and limitations of the major prototyping processes used to fabricate two critical parts of a centrifugal pump: the closed impeller and the volute. These two parts do not operate independently of each other as the volute determines the surroundings in which the impeller operates, and it can have a deep effect on the hydraulic pump performances, causing the impeller to work inefficiently. For a faster validation of the proposed closed impeller and volute design in terms of hydraulic performances, prototypes shall be manufactured using additive manufacturing methods based on plastic materials, to reduce the time needed for producing the corresponding prototypes. However, in order to apply these methods, a trade-off must be carried out between different technologies and materials to identify which additive manufacturing methods offer the most suitable dimensional accuracy, surface quality and tolerances. In this regard, three technologies have been addressed from four different suppliers.

2. DESIGN AND METHODS

A major objective for INCD Turbomotoare COMOTI in the space domain is to qualify a versatile centrifugal pump for MPFL systems, shown in Figure 1, in terms of architecture in order to allow an easy retrofit on future applications (Orion Multi-Purpose Crew Vehicle). In the end the purpose is to have a family of pumps able to work with different working fluids. The overall technical specifications for the MPFL pump are presented in Table 1. Based on the general architecture for the pump and with respect to the imposed requirements, the closed impeller and volute were optimised by means of CFD analyses [10] and further modelled using a CAD software (SolidEdge, version 2019, Siemens PLM Software, Cologne, Germany), as presented in Figure 2.

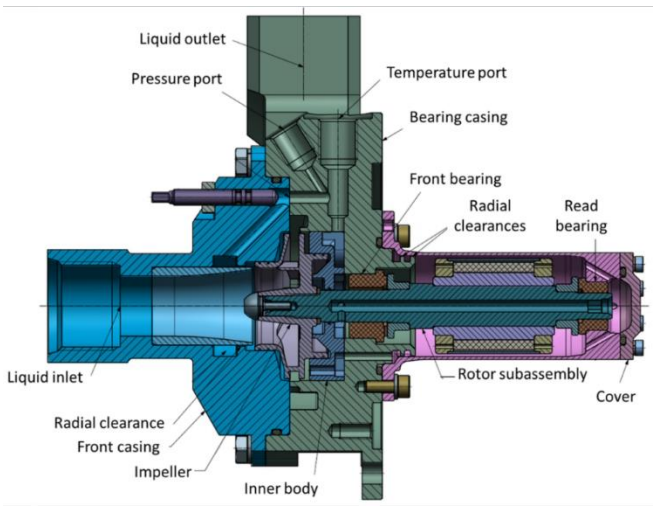

Fig 1. Pump Motor Unit - general architecture

Table 1. Centrifugal pump technical requirements

Working fluid	HFE7200
Flow rate [kg/h]	600-950
Pressure rise [bard]	2÷4
Operating environment temperature range [°C]	-20 to 50
Non-operating environment temperature range [°C]	-30 to 60
Operating life	≥15 years

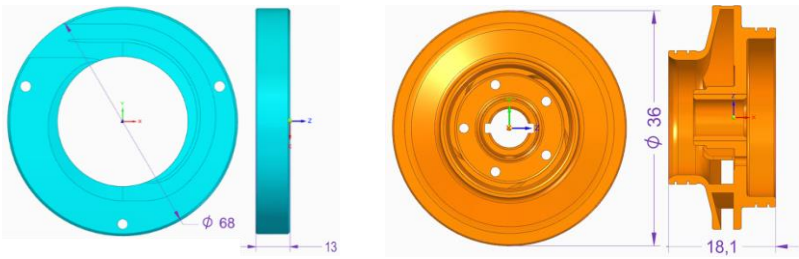

(a) (b)

Fig 2. CAD models for pump components indicating (a) volute and (b) closed impeller

Industrially, there are many types of additive manufacturing methods used, working on different physical principles. According to ISO/ASTM 52900 and ISO/ASTM 52910 [11, 12] these processes were classified in 7 main groups: *binder jetting*, *directed energy deposition*, *material extrusion*, *material jetting*, *powder bed fusion*, *sheet lamination* and *VAT photopolymerization*. For the current study, the SLS method from the powder bed fusion group, SLA method from the VAT photopolymerization group and Polyjet method from material jetting category were chosen. Table 2 summarizes the capabilities and performances of the selected 3D methods. In Table 3 the used material properties are presented, as identified in their data sheet.

Table 2. Plastic additive manufacturing methods selected [13, 14, 15]

Process Parameter	SLA	SLS	Polyjet
Equipment	Formlabs Form 3	Sinterit LISA	Stratasys Polyjet J55 Prime
Layer thickness [µm]	50-100 (HR) 50-150 (SR)	0.075 (HR) 0.175 (SR)	15 (HR) 30 (SR)
Minimum feature size [µm]	1000	750-1000	600-1100
Maximum model size [mm]	150 x 150 x 150	90 x 130 x 230	651 x 661 x 774
Material selection*	Rigid 10 K	PA12 (nylon)	VeroWhitePlus

where, HR-High Resolution, SR-Standard Resolution, Materials suggested by the supplier with respect to the pump technical requirements.

Table 3. Material properties [16, 17, 18]

Material / Properties	Rigid 10 K	PA12 (nylon)	VeroWhitePlus
Applications	Parts with significant loads, aerodynamic test models; heat resistant and fluid exposed components, jigs, fixtures	Detailed printouts, structural or mechanical elements, functional prototypes or final parts.	Highly accurate presentation models, Smaller parts with complex features
Appearance	Liquid, white	Solid, navy grey	White
Physical properties			
Density [g/cm^3]	1.63	0.92	-
Granulation [µm]	-	18-90	16-30

Mechanical properties			
Tensile strength [MPa]	55	41	58
Tensile modulus [GPa]	7.5	-	2.5
Elongation at Break [%]	2	13	10-25
Flexural strength [MPa]	84	-	93
Flexural modulus [GPa]	6	-	2.7
Impact strength (unnotched) [J/m]	41 (IZOD test)	15-20 (Charpy test)	25 (IZOD test)
Shore D hardness	-	74	85

The basic methodology for all the additive manufacturing methods can be summarized as follows:

- The CAD model is created and translated to a STL model using the same software (in current paper both CAD models were translated with a conversion tolerance of 0.001 mm and a surface plane angle of 1°);
- 3D printer software to initialize the printing process based on STL model slicing layers of the model;
- The first layer of the physical model is created. The model is then lowered by the thickness of the next layer, and the process is repeated until completion of the whole model;
- The support structure is removed and finished.

3. EVALUATION AND RESULTS

The dimensional accuracy and surface quality of prototypes has been evaluated comparing the three methods. Surface roughness was measured using a Mahr Surf PS10 instrument (Mahr GmbH, Gottingen, Germany). Dimensional accuracy analysis was performed using a 3D laser surface scanning ATOS Compact Scan 5M machine, integrated with GOM's software for scanning and inspection with $2 \times 5 \times 10^6$ pixels and measuring point distance between 0.017 and 0.481 mm. The correlation between the measured model of the closed impeller/volute and the CAD model was performed by means of three-point alignment. The three alignment points were: axis of rotation; interior surface; thrust balancing holes axis.

3.1. Visual Inspection

After printing phase and support structure removal, each prototype was visually inspected. For the SLA printed components, presented in Figure 3, a pattern on the flow channel of the volute was observed, generated by the scanning strategy (parameter of printing process). In Figure 4 the SLS manufactured pump components are presented. The same pattern, but less noticeable, is visible on the flow channel of the volute. Figure 5 illustrates the volute and the closed impeller manufactures using Polyjet methods. In this case, a smoother pattern is visible only on the side part of the volute channel, not on the top surface. Polyjet parts have the best surface quality and dimensional accuracy, and the results are presented in the following section.

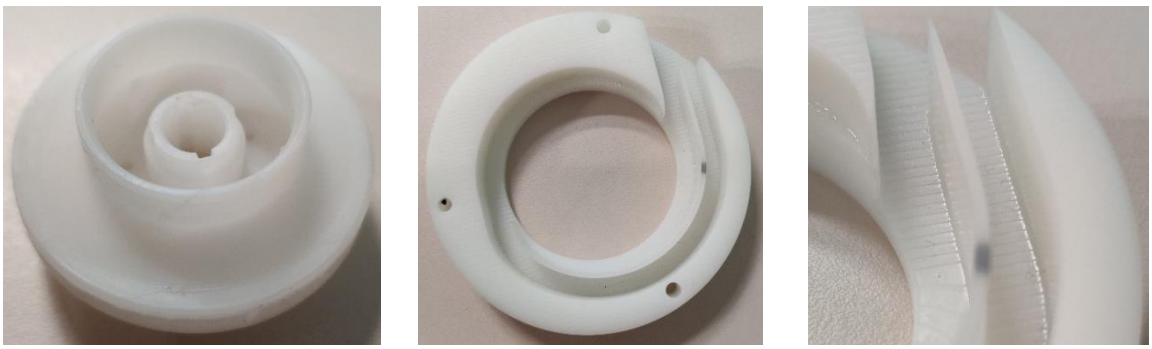

(a) **(b)** **(c)**

Fig 3. Images of SLA manufactured parts for (a) closed impeller, (b) volute and (c) volute channel

(a) (b) (c)

Fig 4. Images of SLS manufactured parts for (a) closed impeller, (b) volute and (c) volute channel

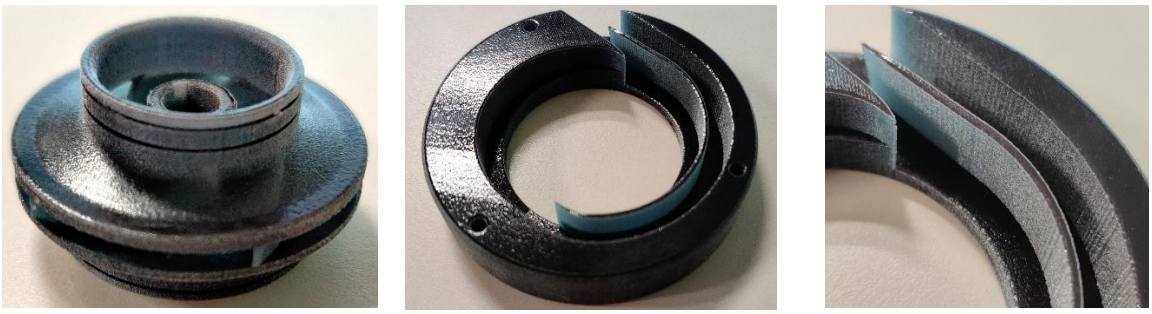

(a) (b) (c)

Fig 5. Images of Polyjet manufactured parts for (a) closed impeller, (b) volute and (c) volute channel

The closed impeller was designed with labyrinths (0.4 mm) on both the front and the rear shroud. During the visual inspection it was observed that these labyrinths were not manufactured properly. Acceptable results were achieved only for the Polyjet method (see Figure 6 c).

(a) (b) (c)

Fig 6. Detailed images of closed impeller labyrinths for (a) SLA, (b) SLS and (c) Polyjet

These prototypes shall be used in a pump demonstrator to verify the hydraulic performances. Due to the draw-backs of these additive manufacturing methods, the labyrinths have to be machined to be in line with the accuracy imposed by the requirements.

3.2. Surface roughness evaluation

The external surface area of each prototype was evaluated and the results are presented in Table 4, as an average value of five measurements. The minimum roughness was found on the SLA volute, 0.965 µm and the maximum on the SLS volute, 11.345 µm. In the case of the closed impeller, best results were achieved for the Polyjet method, 1.789 µm. The SLS impeller remains the part with the highest roughness.

Table 4. Roughness evaluation

Method	Values	Closed impeller		Volute	
		Ra [μm]	Rz [μm]	Ra [μm]	Rz [μm]
SLA	Average value	2.495	19.273	0.965	7.575
	Std. dev.	0.221	1.373	0.402	2.005
SLS	Average value	8.359	56.357	11.345	67.308
	Std. dev.	0.318	1.777	1.191	5.173
Polyjet	Average value	1.789	10.957	1.503	10.266
	Std. dev.	0.598	2.310	0.477	2.743

3.3. Dimensional accuracy evaluation

The dimensional evaluation of the closed impeller prototypes is presented in Figure 7 (a). On the external surface area of the SLA impeller a maximum deviation of 0.139 mm was identified, but on the back of the impeller, the deviations are between 0.259 and 0.517 mm. The dimensional accuracy of SLS closed impeller is worse, between the range of (-0.011 ÷ 0.171) mm on the shroud and (-0.242 ÷ 0.225) mm on the back. The Polyjet manufactured closed impeller presents a very good dimensional accuracy, the deviation range on the shroud being (-0.073 ÷ 0.033) mm and (-0.054 ÷ 0.074) mm on the back.

The section view presented in Figure 7 (b) is pointing out the advantage of the Polyjet method with a dimensional accuracy between (-0.091÷ 0.027) mm. For the SLS part a maximum deviation of 0.262 mm was identified on the blades and -0.096 mm for SLA impeller. The pattern identified on the volute channels and mentioned in Section 3.1 can be also observed in Figure 8. The scanned volute prototypes highlight a maximum deviation of 0.155 mm on SLA volute, 0.917 mm for SLS volute and only 0.086 mm for the Polyjet volute.

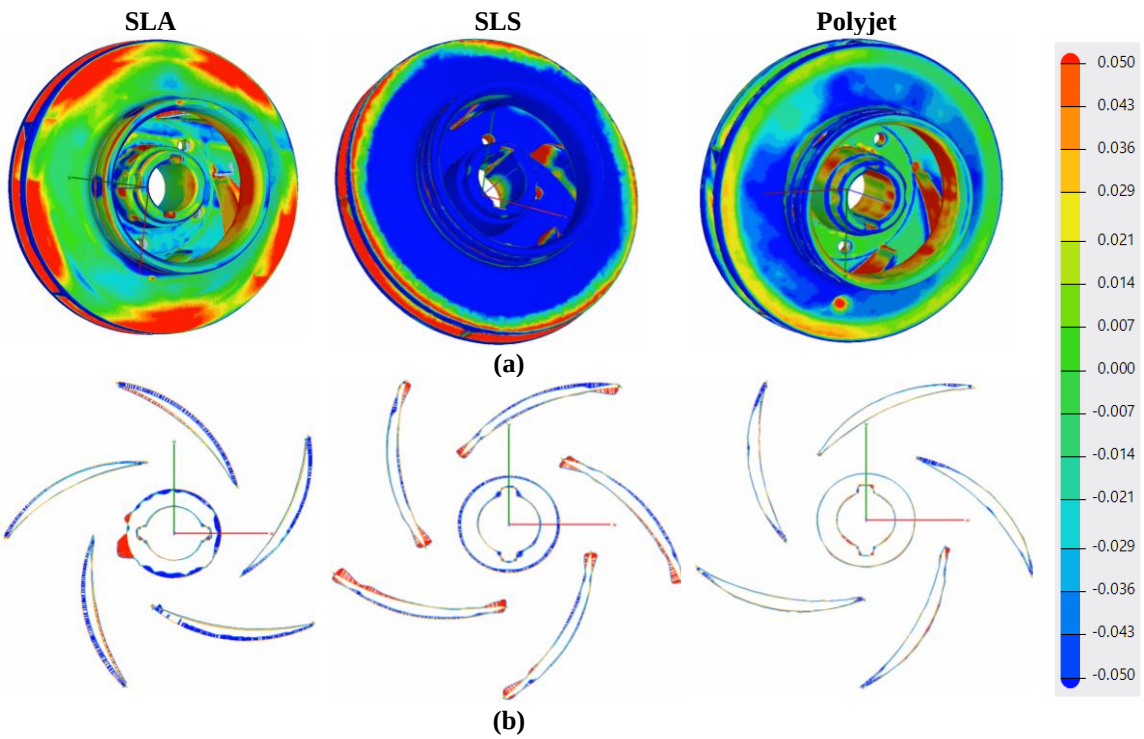

Fig 7. Closed impeller prototypes: (a) Top view, (b) Section view (blades)

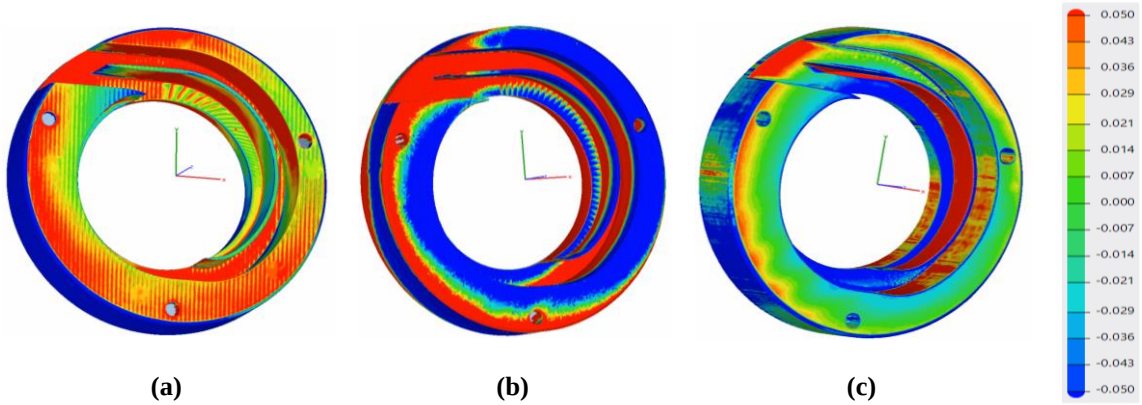

(a) **(b)** **(c)**

Fig 8. Volute prototypes - dimensional evaluation of (a) SLA, (b) SLS and (c) Polyjet

During the dimensional evaluation of the Polyjet volute, a deviation of 0.963 mm was identified between the CAD model and the scanned part. This deviation is located on the volute tongue as illustrated in Figure 9. It is important to mention that the thickness of the volute tongue is only 1 mm (minimum feature size according to Table 2). The deviation appeared as the additive manufacturing process deals with a more flexible material compared to metallic additive manufacturing processes. In order to have a more stable accuracy of the volute tongue, different orientations shall be investigated.

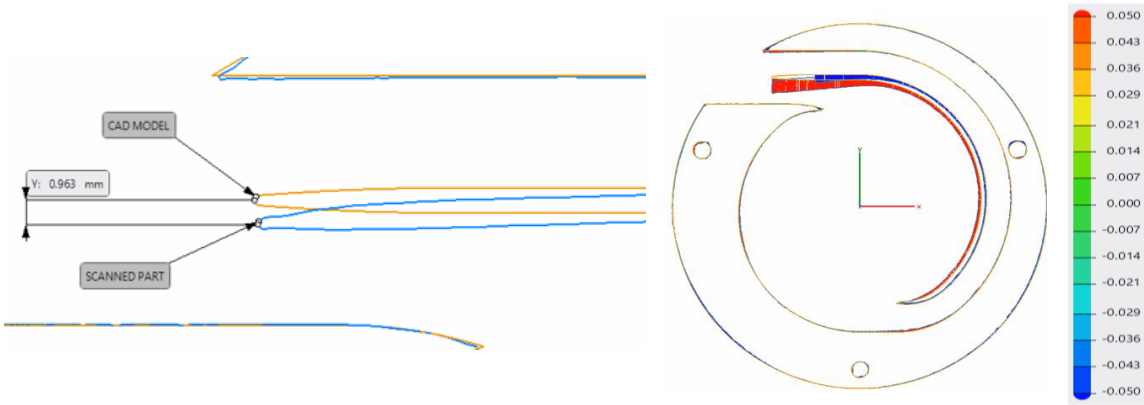

(a) **(b)**

Fig 9. Illustration of (a) detailed image of Polyjet volute tongue deviations and (b) overall accuracy deviation

4. CONCLUSIONS

Additive manufacturing methods are a very useful tool which can accelerate the development process of a product. The working principle of these methods enable to produce and test different technical solutions as complex design models for pump components. It was observed that the surface quality varies from volute and impeller even if both pieces were manufactured with the same methods. This means the geometry of the part has an impact on the surface quality, the more complex the geometry, the higher roughness is achieved. However, the difference between Polyjet volute and impeller is very small. If specific performances are targeted for the prototypes (as hydraulic performances), post-processing methods can be applied to refine the surface (manual or automated depowdering, dyeing or chemical smoothing).

From the dimensional stability point of view, the Polyjet manufactured parts present the smallest dimensional deviations and the labyrinths were manufactured closest to the design model. If required, the labyrinth can be mechanically machined to obtain the best geometrical accuracy and, if necessary, the design of the closed impeller will be optimised for lathe machining to allow the grip of the impeller while machining the labyrinths. It is also important to mention that no offset material was provided and this might be a solution to avoid the deviation of the volute tongue.

Considering the aim of this paper and based on the results presented, it can be concluded that the

Polyjet method represents a solution to evaluate complex design models. SLA methods can be also used for parts which do not require fine details. To assess the identified problems in terms of dimensional stability and roughness, future research should include investigations of different part orientations and providing offset material to avoid features with minimum size of 1 mm and to avoid deviations. Moreover, post-processing operations shall be considered if offset material is added.

In the next development step, the additive manufacturing plastic components will be integrated in a pump demonstrator and its hydraulic performances will be assessed.

REFERENCES

[1] Grand View Research, "3D Printing Plastics Market Size, Share & Trends Analysis Report by Type (Photopolymers, ABS & ASA, Polyamide/Nylon, PLA), By Form (Filament, Ink, Powder), By End-user, By Region, And Segment Forecasts, 2020 - 2027," 04 October 2021. [Online]. Available: https://www.grandviewresearch.com/industry-analysis/3d-printing-plastics-market.

[2] M. Attaran, "The rise of 3-D printing: The advantages of additive manufacturing over traditional manufacturing", Business Horizons, vol. 60, no. 5, pp. 677-688, 2017, https://doi.org/10.1016/j.bushor.2017.05.011.

[3] E. MacDonald and R. Wicker, "Multiprocess 3D printing for increasing component functionality," Science, vol. 353, no. 6307, 201, https://doi.org/10.1126/science.aaf2093.

[4] A. Adiaconitei, I. Vintila, R. Mihalache, A. Paraschiv, T. Frigioescu, M. Vladut and L. Pambaguian, "A Study on Using the Additive Manufacturing Process for the Development of a Closed Pump Impeller for Mechanically Pumped Fluid Loop Systems," Materials, vol. 4, no. 14, 2021, https://doi.org/10.3390/ma14040967.

[5] A. Adiaconitei, I. S. Vintila, R. Mihalache, A. Paraschiv, T. F. Frigioescu, I. F. Popa and L. Pambaguian, "Manufacturing of Closed Impeller for Mechanically Pump Fluid Loop Systems Using Selective Laser Melting Additive Manufacturing Technology," Materials, vol. 14, no. 20, 2021, https://doi.org/10.3390/ma14205908.

[6] I. S. Vintila, A. Adiaconitei, R. Mihalache, A. Paraschiv, T. Frigioescu, F. Condurachi and D. Datcu, "A study on reducing the adherent dross on additively manufactured closed impeller," Scientific Journal TURBO, vol. VIII, no. 1, pp. 33-41, 2021, http://www.comoti.ro/docs/jurnal/Jurnal%20TURBO%20Vol%20VIII%20No%201%202021.pdf .

[7] K. Medhavi and S. Abhishek, "A Comprehensive Study on 3D Printing Technology," MIT International Journal of Mechanical Engineering, vol. 6, no. 2, pp. 63-69, 2016.

[8] L. Bechthold and e. al, "3D printing: A qualitative assessment of applications, recent trends and the technology's future potential", Studien zum deutschen Innovationssystem, vol. 17, 2015.

[9] D. Mahindru and P. Mahendru, "Review of Rapid Prototyping-Technology for the Future," Global Journal of Computer Science and Technology, vol. 13, no. 4, 2013.

[10] Dumitrescu, O., Popa, I.F., Design and optimization of a centrifugal pump as part of mechanically pumped fluid loop cooling system for spacecraft, U.P.B. Sci. Bull., Series D, Vol. 83, Iss. 3, 2021, pp 277-290.

[11] ISO/ASTM 52900, Additive Manufacturing—General Principles—Terminology, 2015

[12] ISO/ASTM 52910, 2017(E) Standard Guidelines for Design for Additive Manufacturing, West Conshohocken, PA: ASTM International, 2017.

[13] Supplier for SLA printing process, Laboratory of Acoustics and Vibrations, National Research & Development Institute for Gas Turbines COMOTI, Bucharest, equipment data sheet access link.

[14] Supplier for SLS printing process, 3DMT Solution, Digital, Manufacturing Technology, access link.

[15] Supplier for Polyjet printing process, NuTechnologies, access link.

[16] Formlabs Rigid 10K resin material data sheet, access link.

[17] Sinterit PA12 powder material data sheet, access link.

[18] Stratasys VeroWhite RGD836 material data sheet, access link.

COMPUTATIONAL AND EXPERIMENTAL STUDY ON DEFECT EMERGENCE IN INVESTMENT CAST COMPRESSOR BLADE FOR INDUSTRIAL GAS TURBINES

Mihaela Raluca CONDRUZ[1], Teodor-Adrian BADEA[1], Tiberius Frigioescu FRIGIOESCU[1], Alexandru PARASCHIV[1], Cornel TODEA[2]

Received: 01.11.2021
Accepted: 10.12.2021
Published: 20.12.2021

Copyright: The article is an Open Access article and it is distributed under the terms and conditions Creative Commons Attribution (CC BY) license (**https://creativecommons.org/licenses/by/4.0/**).

ABSTRACT: The properties and service life of cast parts depend on many factors, including the casting process-induced defects. The present paper is focused on studying the defect emergence in the particular case of an investment cast compressor blade for an industrial gas turbine using additively manufactured wax models. A study on the casting and solidification process was realized using the ProCAST™ software to predict critical areas where defects could emerge. Based on non-destructive testing performed by radiographic inspection and 3D computed tomography, defects like gas-induced porosities and closed shrinkage defects were observed. Overall, the experimental results are in good agreement with the results obtained by computational methods.

KEYWORDS: Investment casting, ProCAST™, compressor blade, material jetting

1. INTRODUCTION

Nowadays, the research in the gas turbine field is focused mainly on aviation gas turbine development and less on industrial gas turbines (IGTs). Even if they are designed for aviation or industrial field, the compressor and turbine blades are one of the most critical components. The blade's performance and durability are derived from material properties, part's shape, and dimensional accuracy. As high precision and dimensional accuracy are imposed for such components, the main technology used for manufacturing is investment casting [1-3].

Investment casting or "lost-wax" casting is one of the oldest manufacturing technologies used for the production of metallic parts. It implies the use of a solid mold or ceramic shells to shape the alloy. From both of the process versions, for industrial applications, ceramic shells are used [4].

The main stages of the investment casting process are wax models manufacturing, pattern tree assembly, slurry coating, stuccoing, dewaxing, firing, casting, ceramic shell knockout, finishing, and inspection [4-6]. Conventionally, the wax models are manufactured by liquid wax injection in metallic molds, but in the last decades, the wax models of prototypes or small series are produced by advanced technologies such as additive manufacturing (AM) [7, 8].

The investment casting process where additive manufactured (AMed) wax models are used is similar to the conventional process except for the first stage, as it can be seen in the graphical representation from Figure 1.

[1] Romanian Research and Development Institute for Gas Turbines COMOTI
[2] SC PLASMATERM SA

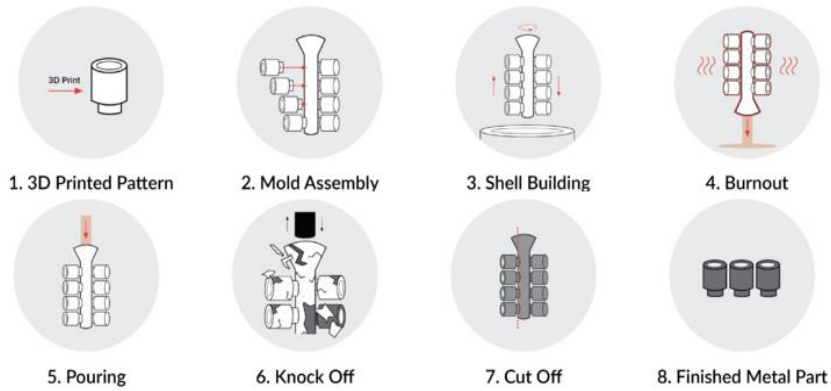

Fig. 1. The investment casting process using 3D printed model [9]

Many defects can result in cast parts during the solidification process and some of them can be eliminated by changing the casting and solidification conditions [10, 11]. To reduce material losses and for a better understanding of the casting process of each designed part, researchers employ computational modeling software. It is recommended to perform a computational study of the casting and solidification process to predict the critical areas of cast parts where defects may form [12, 13]. One software that can be used to perform such simulations is ProCAST^{TM} (ESI Group) [14-16].

In terms of materials, stainless steels are common alloys used in power generation market for manufacturing gas and steam turbine components, especially compressor parts [17-19]. The main goal of the study was to establish the defect emergence in investment-cast compressor blades designed for industrial gas turbines. To achieve the study's aim, computational and experimental methods were applied.

2. MATERIALS AND METHODS

A compressor blade 3D CAD model was designed using SolidEdge ST4 software, as it can be seen in Figure 2. This model was used to manufacture two wax patterns by additive manufacturing (AM) technology, the material jetting (MJ) method. For the manufacturing process, the ProJet 3600W (3D Systems) machine was used, along with the VisiJet M3 Hi-Cast used as building material and VisiJet S400 as support material. The Xtreme High Definition (XHD) printing mode was selected. This printing mode implies a 16 µm layer thickness.

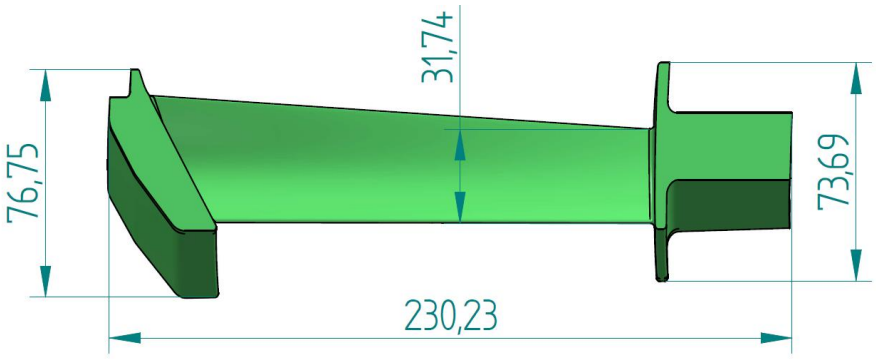

Fig. 2. Compressor blade – 3D CAD model

Wax patterns were detached from the building plate by placing it on the heated platform of a magnetic stirrer Ika C-Mag HS 10 (temperature set at 55°C). The building plate was kept until the support material started to melt and the models were manually removed. All support material removal was ensured by placing the wax models in warm isopropyl alcohol. An open container with isopropyl alcohol, a perforated ceramic plate, and a 40 mm magnet was placed on the heated platform of the magnetic stirrer and the alcohol was heated from room temperature until it reached 40°C. The wax patterns were placed in the container and the stirring process was started using a 900 rpm stirring rate.

After all support material was removed, the patterns were left to dry at room temperature and were attached to a usual casting wax sprue, runner, and gating system in order to form the pattern tree needed to manufacture the ceramic shell. For the assembly, conventional investment casting wax was used (green wax) which is compatible with the wax used for AM process. Table 1 shows the characteristics of both wax systems used for investment casting.

Table 1. Wax characteristics

No.	Parameter	VisiJet M3 Hi-Cast [20]	Conventional green wax
1	Melting point	70°C	84-86°C
2	Softening point	52-62°C	72-75°C
3	Needle Penetration Hardness	9	7-11
4	Ash content	<0.05%	0.05%

Ceramic shells based on colloidal silica and quartz flour were manufactured. An AISI 304 L (X2CrNi18-9) stainless steel batch was melted in an induction melting furnace and was poured in 950°C heated ceramic shells and left to solidify. After solidification, the ceramic shells were destroyed by shot and sandblasting. Once all ceramic material was removed, the sprues were mechanically detached.

To perform the casting and solidification simulation, a 3D CAD model of the pattern tree was realized starting from the compressor blade 3D CAD model. The ProCAST^{TM} software, Casting module was used for computational analysis. The mesh generated in ProCAST^{TM} consisted in 280.360 nodes and 1.729.310 elements (105.946 2D elements, 1.623.364 3D elements). AISI 4820 (17CrNiMo6) stainless steel was selected from the software database to perform the casting simulation, while refractory alumina was selected for the shell. The simulation started at an ambient temperature of 20°C until the casting temperature of 1600°C was reached, further the alloy was poured in 950°C heated shells and the simulation was performed until the part reached 400°C.

For the casting material, the alloy's specific and latent heat values were kept constant all over the simulation process, while a temperature dependent evolution of the thermal conductivity, enthalpy, Newtonian viscosity and fraction solid were used, as can be seen in the images from Figure 3. For the shell material, the latent heat and Newtonian viscosity values were kept constant, while temperature dependent values were used for thermal conductivity and specific heat.

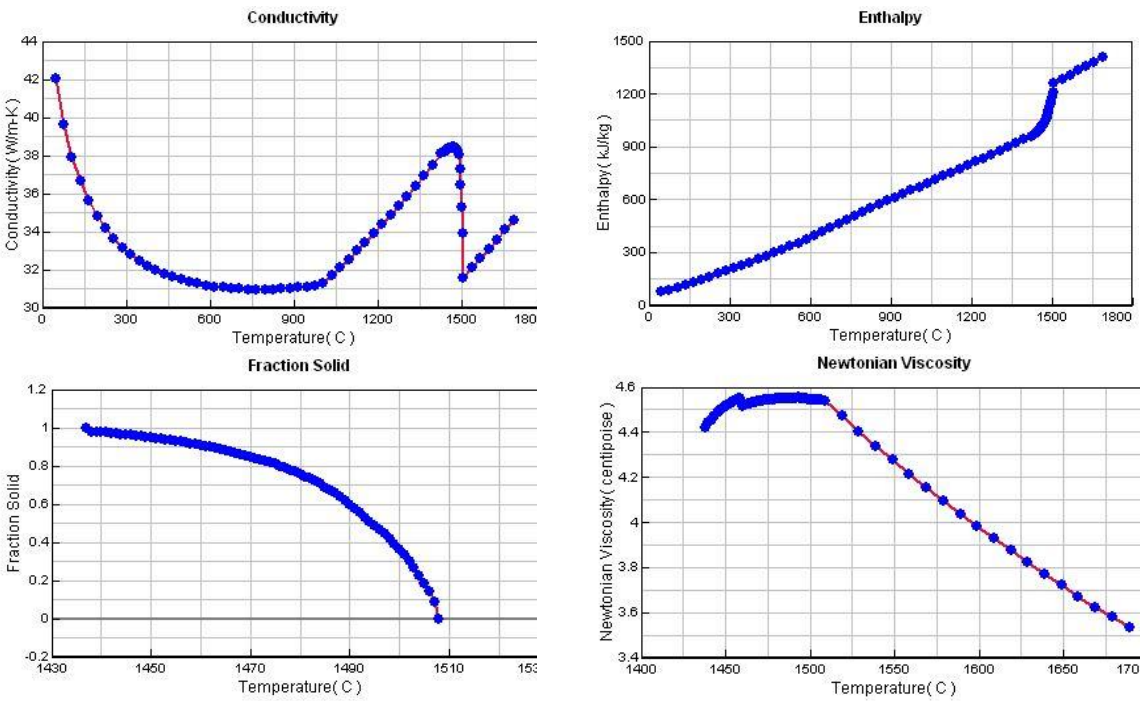

(a) Alloy's characteristics

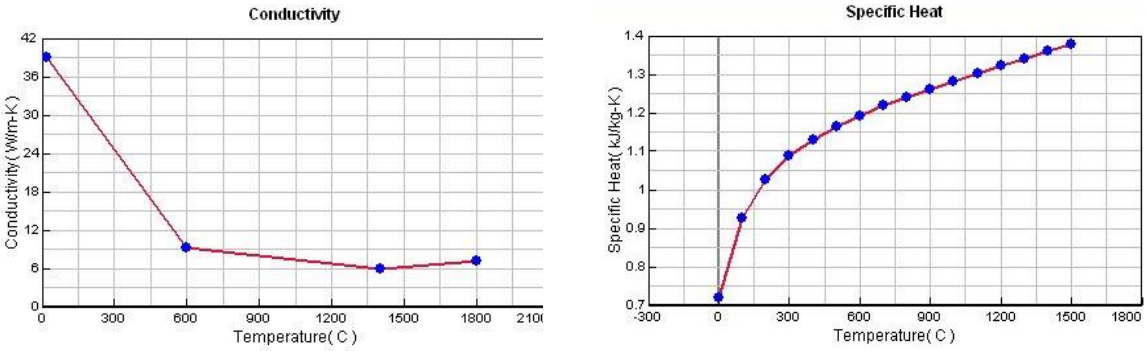

(b) Shell's characteristics

Fig. 3. Conditions imposed for the casting and solidification simulation

The casting induced defects were analyzed after the simulation ended. To validate the simulation results, radiographic inspection and 3D computed tomography (CT) analysis were realized. For radiographic inspection the Seifert ERESCO MF3 portable X-ray unit was used, the analysis was performed using two voltages: 90 kV for the airfoil section and 170 kV for the platforms, 4.5 mA current, and 800 mm source distance to the object.

The CT scan was performed using the Nikon XT H 225 ST equipment and the results were analyzed using MyVGL software from Volume Graphics.

3. RESULTS AND DISCUSSIONS

3.1. Casting and solidification process simulation

In Figure 4 is presented the mesh realized for the pattern tree and shell used for simulation. An interface was created between the pattern tree and the shell, as they are realized by different materials, the COINC option was selected and the heat transfer coefficient between the interfaces was selected at 500W/m^{2}K. A cylindric geometry was selected for the environmental boundary and a coarse mesh was realized for this volume.

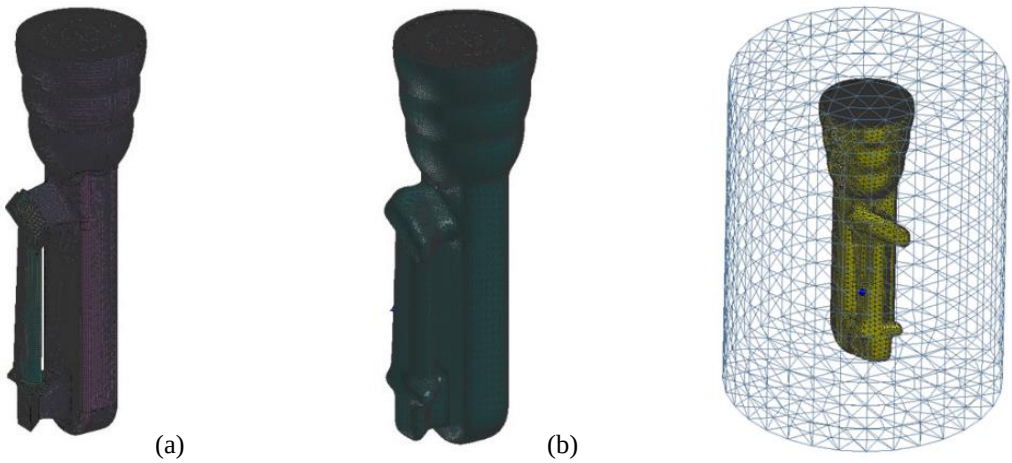

(a) (b) (c)

Fig. 4. Model used for solidification simulation: a) pattern tree's mesh; b) shell's mesh; c) environmental boundary conditions

After all simulation conditions were imposed, the casting process was started. The alloy pouring and shell filling process can be observed in Figure 5 while the temperature distribution as the ceramic shell is filled can be observed in Figure 6.

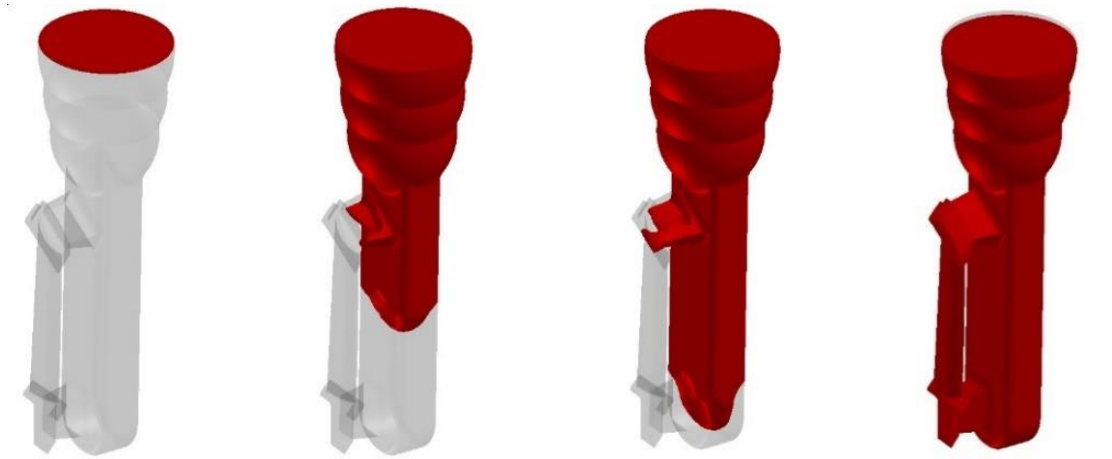

Simulated time: 0.000 s Percent filled: 0.0 Fraction solid: 0.0 | **Simulated time: 0.1349 s Percent filled: 76.2 Fraction solid: 0.0** | **Simulated time: 0.1599 s Percent filled: 90.3 Fraction solid: 0.0** | **Simulated time: 0.1739 s Percent filled: 98.0 Fraction solid: 0.0**

Fig. 5. Alloy pouring and shell filling

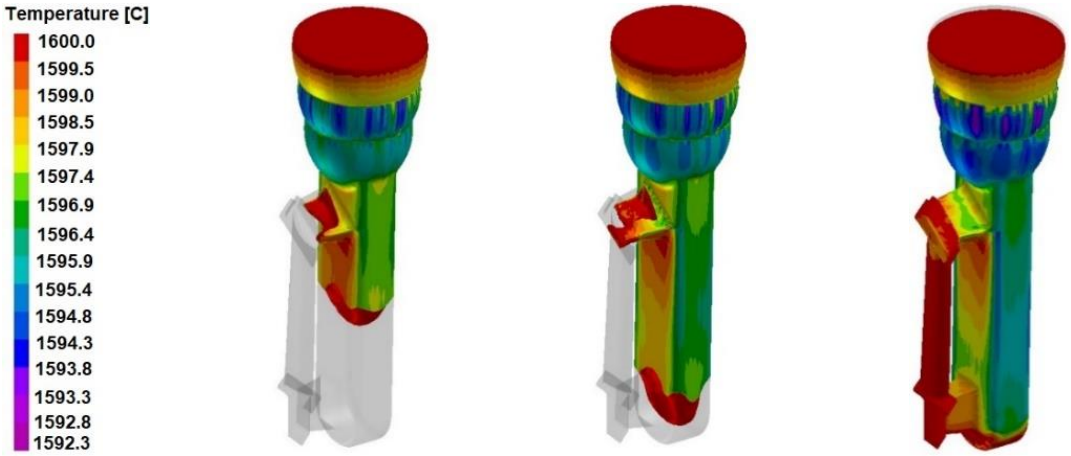

Simulated time: 0.1349 s Percent filled: 76.2 Fraction solid: 0.0 | **Simulated time: 0.1599 s Percent filled: 90.3 Fraction solid: 0.0** | **Simulated time: 0.1739 s Percent filled: 98.0 Fraction solid: 0.0**

Fig. 6. The temperature distribution during shell filling

For AISI 4820 ProCAST^{TM} predicted a liquidus temperature of 1508°C and a solidus temperature of 1437°C. As the pattern tree is characterized by sections with different geometries, some areas reach the solidus temperature faster than other sections, as it can be observed in Figure 7. Even if the airfoil section is the last to fill, it reaches the solidus temperature faster than the sprue, the runner and the gating system because it has a reduced thickness.

ProCAST^{TM} provides also the evolution of temperature during the part solidification. Representative images that show this evolution can be observed in Figure 8. The blade is the first that solidifies as it can be observed from the images from Figure 8 and Figure 9, and the sprue is the last to solidify as its goal is to provide liquid alloy during the solidification to reduce the shrinkage porosities.

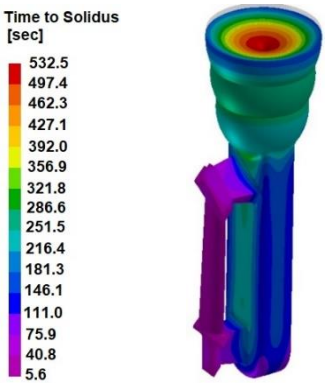

Fig. 7. Time to solidus in different part sections

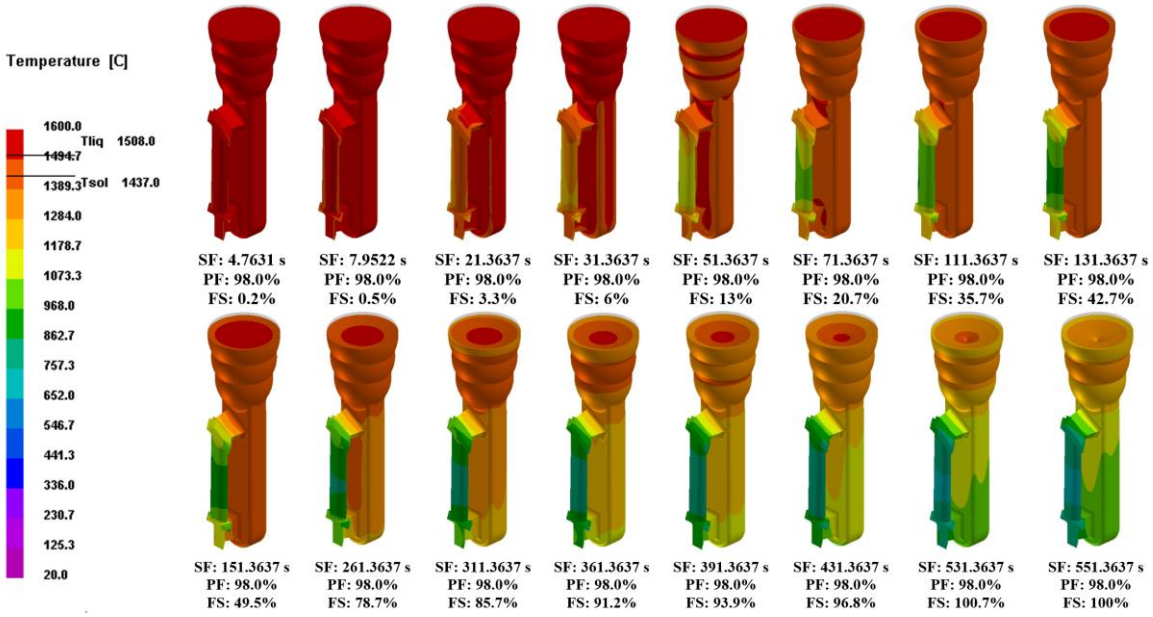

Fig. 8. Temperature distribution during the solidification process (where SF is the solidification time, PF is the percent filled, FS is the fraction solid)

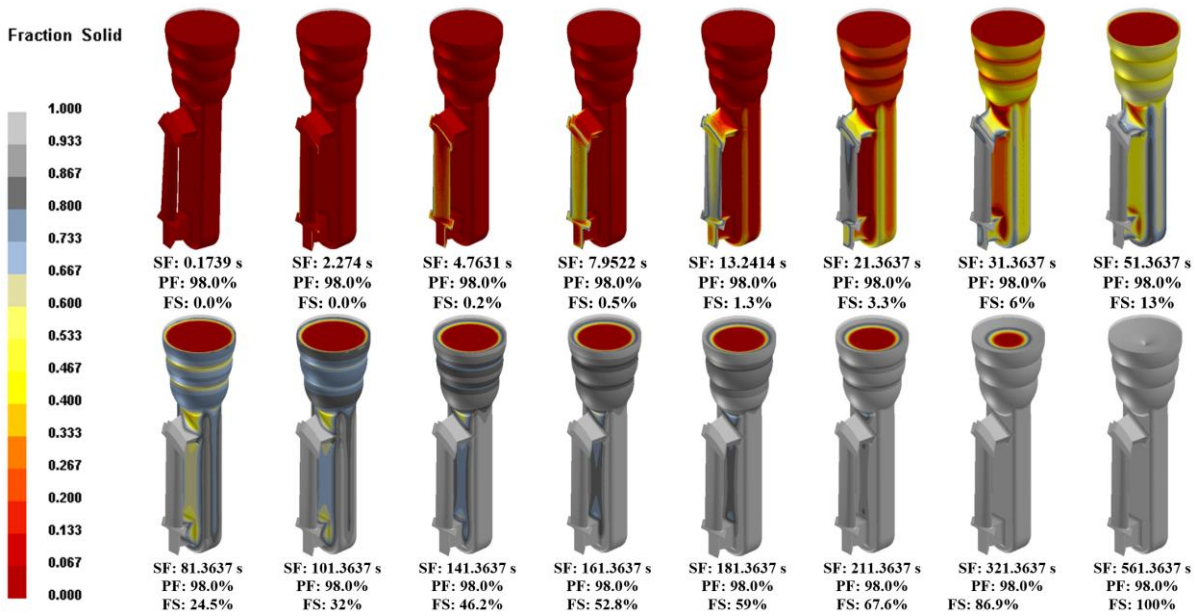

Fig. 9. Solid fraction evolution during the solidification process (where SF is the solidification time, PF is the percent filled, FS is the fraction solid)

After the solidification process was ended, an analysis of the defects resulted in the cast part was realized. The Niyama criterion (Ny) predictions show the areas that are more prone to present porosities caused by material shrinkage during the solidification. The results are presented in Figure 10. This criterion doesn't provide the actual porosity amount, but it gives some qualitative information regarding the most critical areas where it can develop, the lower the Ny value the higher the porosity level is predicted. The image from Figure 10b shows that the most critical area is the center of the airfoil, where Ny values registered were under 15.3 $(K.s)^{1/2}$/cm based on the scale provided by the software. The results reported by other authors in case of steel and nickel-based alloys indicate a critical minimum Ny values of Ny=0.1-1.0 $(°C.s)^{1/2}$/mm for macroscopic defects and Ny=2.0-3.0 $(°C.s)^{1/2}$/mm for microscopic defects [21].

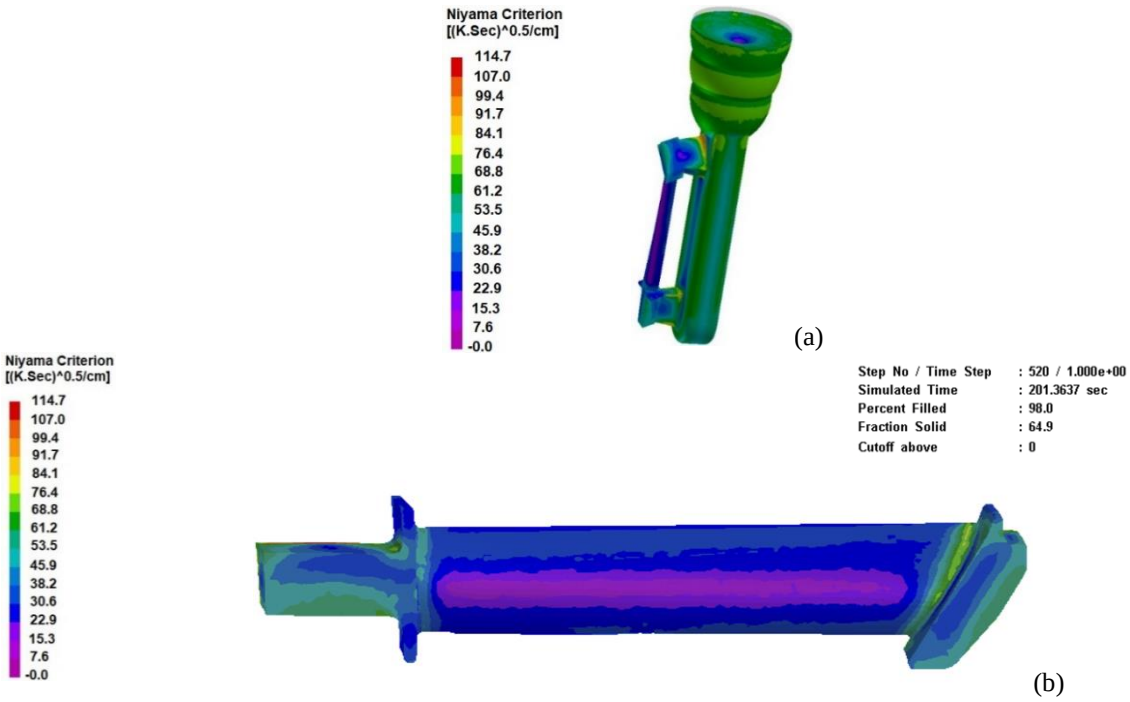

Fig. 10. Ny criterion at the end of solidification process: a) in all pattern tree; b) in the compressor's blade

The shrinkage porosity analysis showed many closed porosities in the compressor blades as well as in the sprue, the runner and in the gating system (Figure 11a). In Figure 11b can be observed the shrinkage porosity level in the blade. A shrinkage porosity level under 1.25% was registered in many blade's sections (in the center of the airfoil and in both platforms). Even if porosity was identified in the compressor blade, no hot spots were predicted.

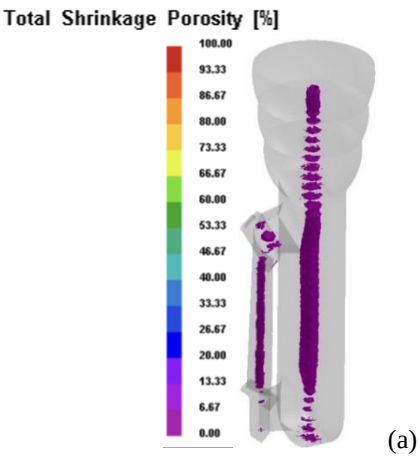

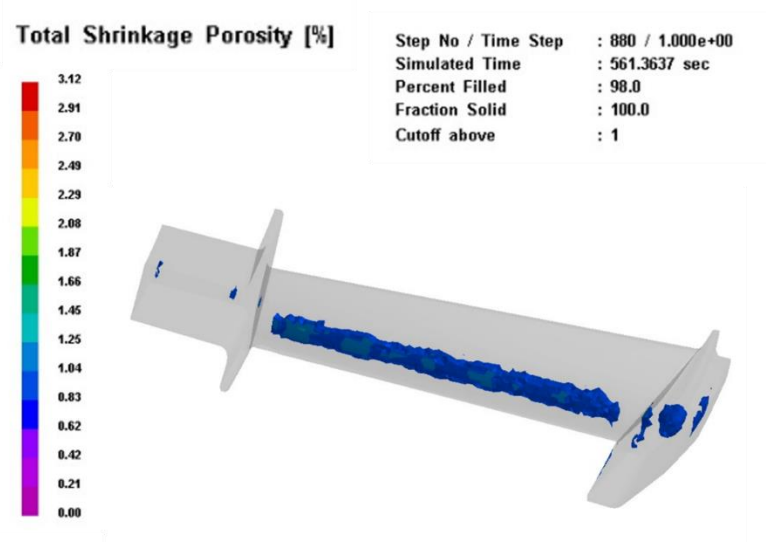

(b)

Fig. 11. Shrinkage porosity resulted in the investment cast part: a) total shrinkage porosity in the pattern tree; b) the shrinkage porosity registered in the compressor's blade

3.2. Compressor blade manufacturing

The investment casting technology implies the use of wax patterns for the ceramic shell manufacturing. Usually, these patterns are made by wax injection in metallic molds, but for the present experiment another method was applied for wax pattern manufacturing, the MJ method. Figure 12 presents the AMed blade wax patterns, where the navy-blue material is the building material and the white material is the support material.

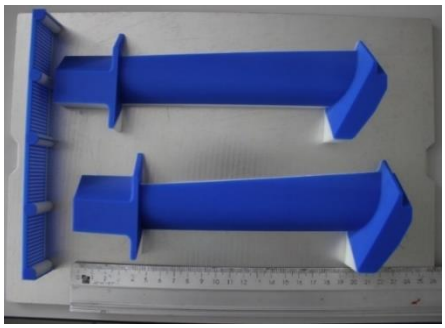

Fig. 12. AMed wax models

Representative images with the wax patterns before and after support material removal are presented in Figure 13. After the patterns were left to dry at room temperature the pattern tree was assembled (Figure 14).

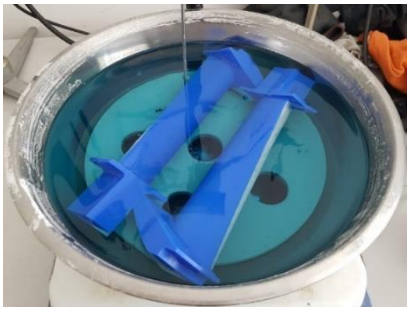

(a)

(b)

Fig. 13. Wax models during (a) and after (b) the support material removal

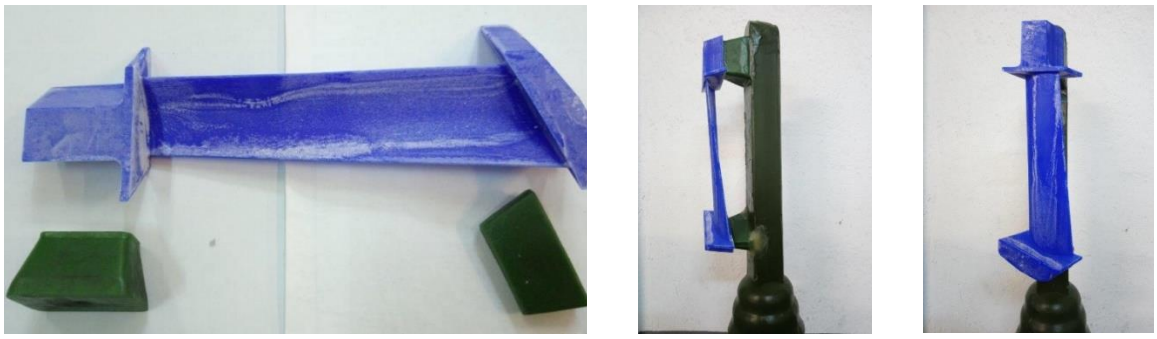

Fig. 14. Pattern tree used to manufacture the ceramic shell

After the pattern tree was assembled, it was dipped in the slurry coating made from colloidal silica and quartz flour and in stuccoing based on sand quartz. Different sand grits were used for stuccoing, and many coatings were applied to form a thick ceramic shell. After applying each coating and stuccoing layer the shell was left to dry for 12 h in a drying tunnel in controlled environment (23°C and relative humidity of 50%). Images during the slurry coating and stuccoing are presented in Figure 15.

(a) (b) (c) (d)

Fig. 15. Ceramic shell manufacturing: a) slurry coating; b, c) stuccoing using quartz sand with different grit; d) ceramic shells

When all layers were completely dry, the wax was removed using a steam autoclave (100°C steam's temperature). Once the wax was removed, the ceramic shells were placed in sand metal boxes and were heated until 950°C in order to remove the residual moisture and wax and to sinter the shell. Simultaneously, the AISI 304L stainless steel was melted using an induction melting furnace and it is poured into the hot ceramic shell. After pouring, the solidification process started and once it was finished and the ceramic shells reached the room temperature, they were destroyed by shot and sand blasting. The solidified pattern tree can be observed in Figure 16a. The sprue, runner and gating system were mechanically removed and the investment cast blade can be observed in Figure 16b.

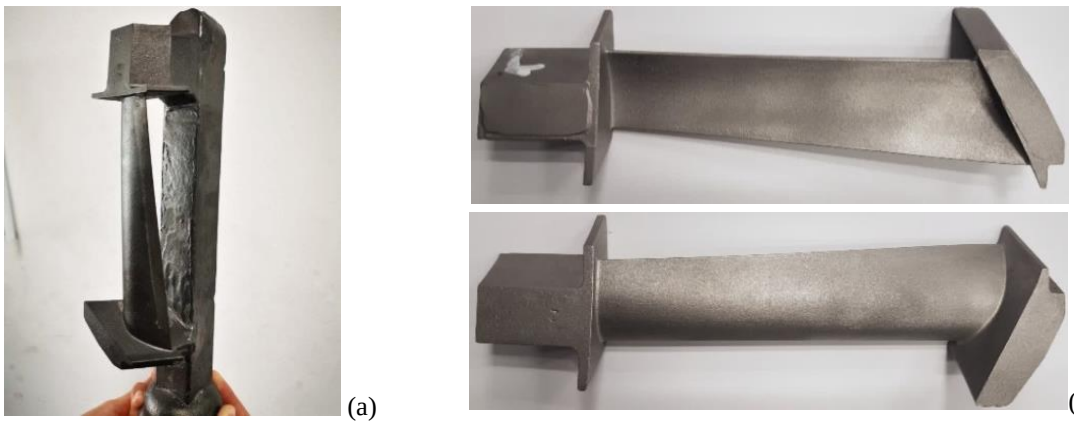

(a) (b)

Fig. 16. Compressor blade experimental model before (a) and after (b) casting elements removal

3.3. Non-destructive testing

Radiographic inspection revealed micropores in the cast blade (marked with red arrows in Figure 17). Moreover, the radiographies showed that the airfoil section is characterized by a reduced densification. It seems that the material was deposited in successive layers that are perpendicular to the airfoil axis as can be seen in the image presented in Figure 17.

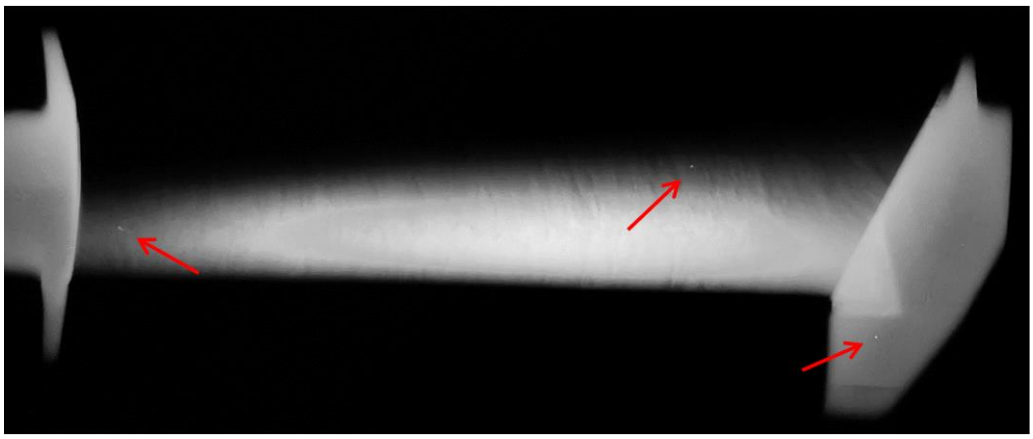

Fig. 17. Radiography of the compressor blade's airfoil

The CT scanning was realized on both platforms and the airfoil. No significant defects were registered for the platforms, but analyzing the airfoil in many sections starting from its base, many closed porosities were observed. A closed porosity is a non-connected cavity formed in the part during the solidification process and it is observed as a black spot in the CT scanning images. The closed porosities can have different morphologies depending how they developed, as a result of gas entrapment or material shrinkage during solidification process. Representative images with the closed porosities are presented in Figure 18.

Based on the results of the CT scanning (Figure 18), it can be said that the airfoil of the compressor blade (center of the airfoil) is the part's critical area, where most of the defects formed. The same critical area was determined by computational methods, but to a higher extent. Larger defects were encountered near one of the platforms as porosities are trapped in the area and cannot be evacuated in this configuration of casting pattern.

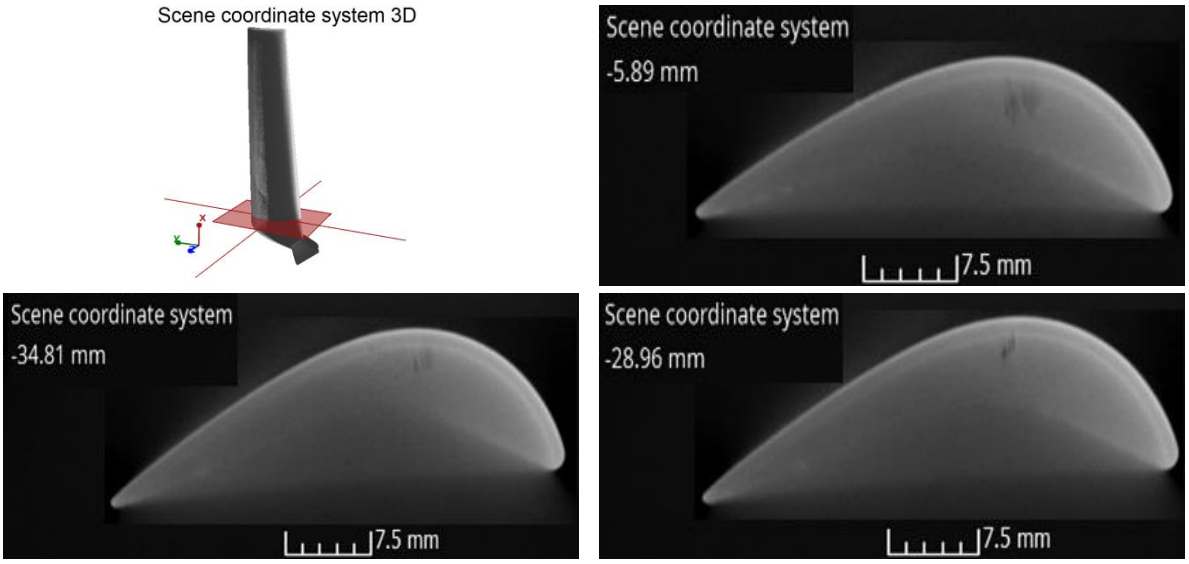

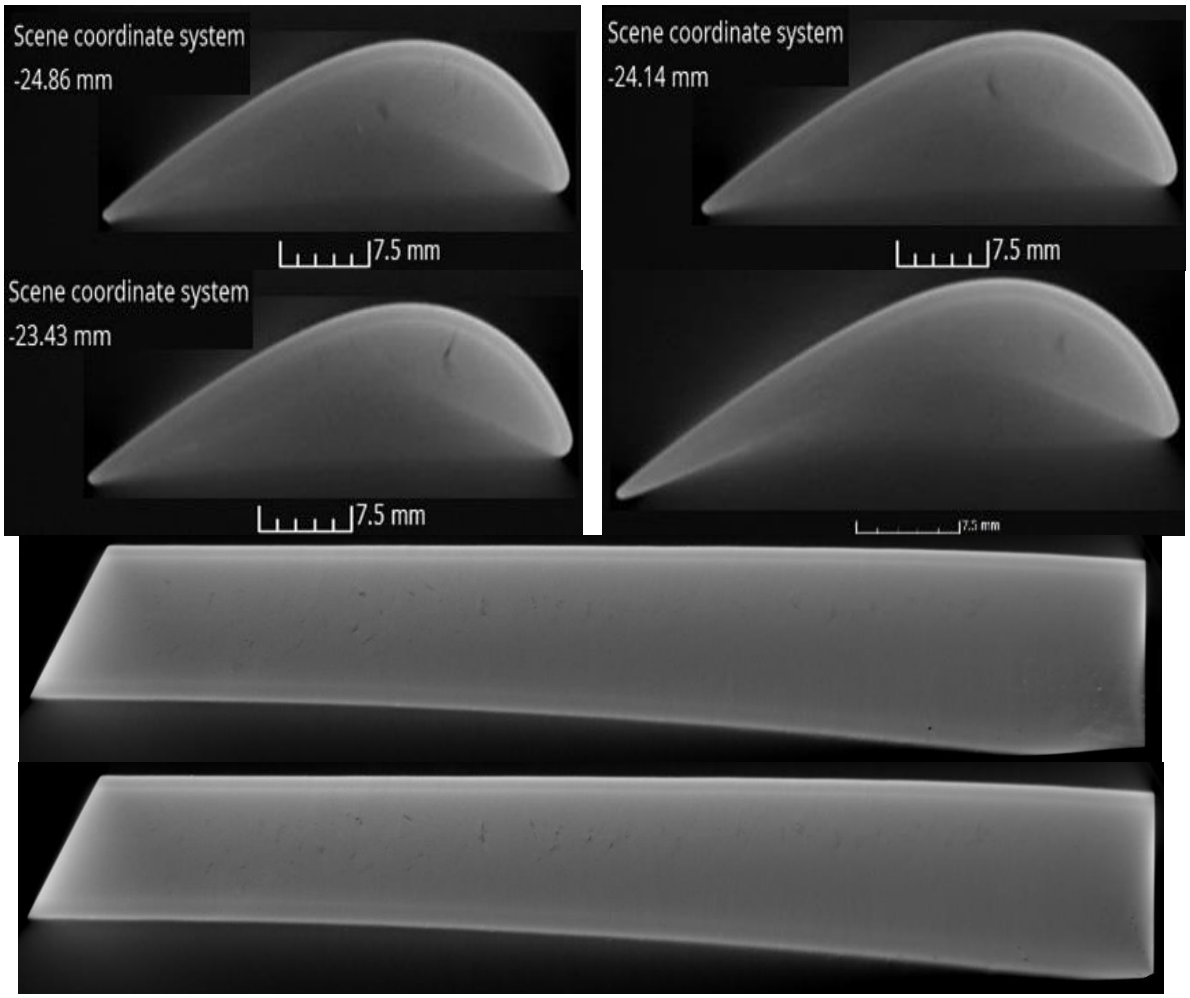

Fig. 18. Representative images with defects highlighted by CT scanning

4. CONCLUSIONS

The present study was focused on studying the defects formed in an investment-cast compressor blade. The analysis was realized both by computational and experimental methods. Compressor blades were cast from stainless steel in ceramic molds.

The wax patterns used for ceramic shell manufacturing were additively manufactured by the material jetting method. The casting and solidification simulation realized using ProCAST™ software revealed that shrinkage porosity forms mainly in the airfoil section of the blade, but also in the center of the platforms.

Non-destructive analyses of one cast part were realized to assess the defect emergence. Two techniques were applied to reveal the casting defects. The radiographic analysis showed that the blade's airfoil is characterized by reduced densification that can diminish the part's mechanical performances and can reduce its lifetime under operation. The CT scanning analysis showed many closed porosities that developed especially in the central area of the blade's airfoil confirming the simulation results, even if experimentally they are formed to a lower extent.

Based on all the results obtained it can be said that the ProCAST™ software can be applied to predict the casting defects emerged during the solidification of investment cast compressor blades.

To reduce the defect percentage or even eliminate it, different solidification conditions should be applied (the ceramic shell and pouring temperature should be controlled). Future studies will be realized to investment cast compressor and turbine blades free of defects and with cooling passages.

ACKNOWLEDGEMENT

This work was carried out within POC-A1-A1.2.3-G-2015, ID/SMIS code: P_40_422/105884, "TRANSCUMAT" Project, Grant no. 114/09.09.2016 (Subsidiary Contract no. 6/D.1.4/114/18.06.2018), Project supported by the Romanian Minister of Research and Innovation. The authors acknowledge to Florin Samoilă from TOP Metrology SRL, Bucharest, Romania for the CT scanning analysis.

REFERENCES

[1]. Zhang D., Cheng Y., Jiang R., Wan N.; 2020, Introduction; Eds. Zhang D., Cheng Y., Jiang R., Wan N.; *Turbine Blade Investment Casting Die Technology*, Springer, Berlin, Heidelberg, pp. 1-20, DOI: 10.1007/978-3-662-54188-3

[2]. Holland S., Dahmen C., Bührig-Polaczek A.; 2008; Gas Turbine Blade made on FG75 – Investment Casting Technology for Complex, Hollow, Fibre-Reinforced NiAl-Components, *Superalloys 2008*, Eds. R.C. Reed, K.A. Green, P. Caron, T.P. Gabb, M.G. Fahrmann, E.S. Hyron, S.A. Woodard, TMS, Pittsburgh, Pennsylvania, USA, pp. 229-238, DOI:10.7449/2008/SUPERALLOYS_2008_229_238

[3]. Lu Z.L., Cao J.W., Jing H., Liu T., Lu F., Wang D.X., Li D.C.; 2013; Review of main manufacturing processes of complex hollow turbine blades, *Virtual Physical Prototyping*, vol. 8, issue 2, pp. 87-95 https://doi.org/10.1080/17452759.2013.790600

[4]. Prasad R.; 2012; Progress in Investment Castings, Ed. Srinivasan M; *Science and Technology of Casting Processes*, IntechOpen, pp. 25-72, DOI: 10.5772/50550

[5]. Singh R., Singh S., Hashmi M.S.J.; 2016; Investment Casting, Ed. Hasmi S.; *Reference Module in Materials Science and Materials Engineering*, Elsevier, Oxford, UK, pp. 1-18, DOI: 10.1016/B978-0-12-803581-8.04163-1

[6]. Fritz J.E., Investment Casting Process, https://www.investmentcasting.org/uploads/8/1/9/8/81988734/the_investment_casting_process_-_website.pdf

[7]. Safaeian D., Vaezi M.; 2009; Investment Casting of Gas Turbine Blade by Used of Rapid Technologies, *Australian Journal of Basic and Applied Sciences*, vol. 3, issue 3, pp. 2979-2988, ISSN1991-8178,

[8]. Wang J., Sama S.R., Lynch P.C., Manogharan G.; 2019; Design and Topology Optimization of 3D-Printed Wax Patterns for Rapid Investment Casting, *Procedia Manufacturing*, vol. 34, pp. 683-694, https://doi.org/10.1016/j.promfg.2019.06.224

[9]. https://www.3duke.co.nz/blog/post/32007/Metal-Casting-3D-Printed-Parts/

[10]. Ingle V., Sorte M.; 2017; Defects, Roots Causes in Casting Process and Their Remedies: Review, *International Journal of Engineering Research and Application*, vol. 7, issue 3, pp. 47-54, DOI: 10.9790/9622-0703034754

[11]. Mane V.V., Sata A., Khire M. Y.; 2011; New Approach to Casting Defects Classification and Analysis Supported by Simulation, *Proceeding of the 59th Indian Foundry Congress*, Chandigarh, India, pp. 87–104,

[12]. Brůna M., Bolibruchová D., Pastirčák R.; 2017; Numerical Simulation of Porosity for Al Based Alloys, *Procedia Engineering*, vol. 177, pp. 488 – 495, https://doi.org/10.1016/j.proeng.2017.02.250

[13]. Kumar R., Madhu S., Aravindh K., Jayakumar V., Bharathiraja G., Muniappan A.; 2020; Casting design and simulation of gating system in rotary adaptor using procast software for defect minimization, *Materials Today: Proceedings*, vol. 22, issue 3, pp. 799–805, https://doi.org/10.1016/j.matpr.2019.10.156

[14]. Zhang S., Xu Z., Wang Z.; 2017; Numerical modeling and simulation of water cooling-controlled solidification for aluminum alloy investment casting, *The International Journal of Advanced Manufacturing Technology*, vol. 91, 2017, pp. 763-770, https://doi.org/10.1007/s00170-016-9808-5

[15]. https://www.esi-group.com/products/casting

[16]. Abhilash E., Joseph M. A.; 2009; Modelling and Simulation of Casting Process: an Overview, *Indian Foundry Journal*, vol. 55, no. 10, pp. 28-37

[17] Brown, R.N.; 2005; Axial Compressors, *Compressors: Selection and Sizing*, Elsevier Science & Technology Books, pp. 262 - 294

[18] Noh M.M., Khattak, M.A., Tamin M.N., Khan, M.S., Iqbal, N., Kosnan, M.S.E., Kazi, S., Khan, M., Subhani. T., Anwar, M.; 2016; Effect of Artificially Produced Pit-Like Defects on the Fatigue Life (S-N Curve) of AISI 410 Stainless Steel Compressor Blades Material, *Journal of Advanced Research in Materials Science*, vol. 17, no. 1, pp. 10-17

[19] Singh, K.; 2014; Advanced Materials for Land Based Gas Turbines, *Transactions of the Indian Institute of Metals*, vol. 67, pp. 601-615

[20] 3D Systems, VisiJet M3 Hi-Cast & CAST RealWax data sheet

[21] Carlson K.D., Beckermann C.; 2010; Development of Thermophysical Property Datasets, Benchmark Niyama Results, and A Simulation Qualification Procedure, in *Proceedings of the 64th SFSA Technical and Operating Conference*, Paper No. 5.5, Steel Founders' Society of America, Chicago, Illinois, USA

On March 1978
Dumitru PRUNARIU
was selected for the
Intercosmos
Program.

On 14 May 1981
he was
the first Romanian
which
flew in space!

COMOTI

The only specialized company that integrates such activities as

scientific research,
design,
manufacturing,
testing,
experimental activities,
technologic transfer and innovation

in the field of aircraft and industrial gas turbines and high speed bladed machinery.

220D Iuliu Maniu Ave., 061206 Bucharest, ROMANIA,
P.O. 76, P.O.B. 174
Phone: (+4)021/434.01.98, (+4)021/434.02.31, (+4)021/434.02.40
Fax: (+4)021/434.02.41, e-mail: contact@comoti.ro

www.comoti.ro